Bifurcation Analysis of a Nose Landing Gear System

I. Tartaruga* ,
Siemens, 3001 Leuven, Belgium

M. H. Lowenberg†, J. E. Cooper‡ and P. Sartor§,
University of Bristol, Bristol, BS8 1TR, UK

Y. Lemmens¶
Siemens, 3001 Leuven, Belgium

Submitted for inclusion in the special session for the ALPES Aircraft Loads Prediction Workshop.

A methodology is proposed to enable the bifurcation analysis of a multi-body nose landing gear (NLG) model by coupling AUTO, a continuation software, to LMS Virtual.Lab Motion, a multi-body software. The approach uses a Singular Value Decomposition (or High Order Singular Value Decomposition) based technique to enable the computation of the stability bounds (e.g. the onset of shimmy) in a very efficient manner. Sensitivity and uncertainty analyses are performed to determine the influence of various structural parameters on the onset of shimmy. A representative aircraft landing gear model was used to validate the approach and it was demonstrated that a good comparison with full-scale Monte-Carlo time simulations was achieved with a much reduced computational expense.

Nomenclature

α_i	tyre lateral slip angle
β	landing gear longitudinal degree of freedom
δ	landing gear lateral degree of freedom at the revolute joint between main fitting and the fuselage
Δ	landing gear lateral degree of freedom at the revolute joint between wheel axis and the trail body
γ_i	camber angle
Ω_i	angular velocity of the wheel
σ_{α_i}	relaxation length adopted for the lateral slip
ρ	air density
ρ_z	overall normal deflection
σ_k	relaxation length adopted for the longitudinal slip
ξ_i	general angle used in the load-expression adopting the *Magic Formula* model
ψ	landing gear torsional degree of freedom
a	half track width
B, C, D, E, S	coefficients of the general expression of a generalized force adopting the *Magic Formula* model
B_m	distance between the centre of gravity of the aircraft and the main assembly
B_n	distance between the centre of gravity of the aircraft and the nose assembly
B	distance between the nose and the axis of the main assembly
C_L	aircraft global lift coefficient
e	caster length
$F_{nominal}$	the nominal wheel load
F_{x0_i}	longitudinal force acting at the tyre contact point with the ground and due to a pure longitudinal slip
F_{x_i}	longitudinal force acting at the tyre contact point with the ground and due to a combined slip
F_{y0_i}	lateral force acting at the tyre contact point with the ground and due to a pure lateral slip

*Marie Curie early stage PhD researcher, ALPES Project, Dept of Aerospace Engineering, University of Bristol, Bristol, BS8 1TR, UK, E-mail: irene.tartaruga@bristol.ac.uk.

†Professor of Flight Dynamics, Dept of Aerospace Engineering, E-mail: M.Lowenberg@bristol.ac.uk.

‡Royal Academy of Engineering Airbus Sir George White Professor of Aerospace Engineering, Dept of Aerospace Engineering, E-mail: j.e.cooper@bristol.ac.uk.

§Lecturer in Aerospace Engineering, Dept of Aerospace Engineering, E-mail: pia.sartor@bristol.ac.uk.

¶Sr Project Leader RTD, E-mail: yves.lemmens@siemens.com.

F_{y_i}	lateral force acting at the tyre contact point with the ground and due to a combined slip
F_{z_i}	Normal load acting at the tyre contact point with the ground
k_i	tyre longitudinal slip
h_i	tyre contact patch
$l_\delta = l_\beta$	gear length
L	lift
M_{x_i}	overturning couple
M_{y_i}	rolling resistance moment
M_{z0_i}	aligning torque due to a pure lateral slip
M_{z_i}	aligning torque due to combined slip
r_0	unloaded radius of the wheel
r_1	loaded radius of the wheel
S	reference surface area of an aircraft
u_i	longitudinal displacement characterizing the tyre dynamics
v_{α_i}	lateral displacement characterizing the tyre dynamics
V_0	reference velocity
V_{x_i}	centre longitudinal velocity
V_{r_i}	forward speed of rolling
V_{s_i}	slip velocity at the wheel slip point
V_{c_i}	magnitude of the velocity of the wheel contact centre C
V_{cx_i}	longitudinal velocity of the wheel contact centre C
V_{cy_i}	lateral velocity of the wheel contact centre C
V_{sx_i}	longitudinal component of the slip velocity
V_{sy_i}	lateral component of the slip velocity
$\overline{W}_n$	vertical load experience by the nose landing gear
V	forward velocity of an aircraft
V	forward velocity of aircraft
W	weight of aircraft
W_{LG}	weight of the nose landing gear
$()_i$	subscript for the ith wheel

MDO	Multidisciplinary Optimization
FEM	Finite Element Method
LCO	Limit Cycle Oscillation
UQ	Uncertainty Quantification
SA	Sensitivity Analysis
SVD	Singular Value Decomposition
HOSVD	High Order Singular Value Decomposition
SV_V, SV_F	Retained Singular Values for forward velocity and load
MCS	Monte Carlo Simulation

I. Introduction

Aircraft landing gear are both a structure and system. It is a complex system with controlled articulation, multiple axes of energy absorption and the sole structure supporting the aircraft on the ground. The main functions of the landing gear are to support the aircraft on the ground, absorb energy during landing, taxiing and braking, as well as to provide directional control. The design of the landing gear is an iterative process which takes into account aircraft configuration, landing gear geometry, static, dynamic and fatigue loads, and structural sizing based on the critical load cases[1,2].

Shimmy is a phenomenon that can occur in all systems with wheels that interact with the ground, and it takes the form of a bounded oscillation e.g. a Limit Cycle Oscillation (LCO)[3] resulting from the interactions of a flexible system with tyre follower forces. Shimmy is a very important consideration for the design of landing gear systems as it can be dangerous and lead to structural failure; however for modern aircraft designs it mainly causes vibration, discomfort and possible fatigue problems. Nose landing gear are prone to shimmy because of the nose wheel steering system which allows the landing gear to move torsionally. Therefore, it is usual in the aerospace industry to investigate the effect of different structural and system parameters through extensive numerical simulations using Multi-Body dynamics models. However, the design needs to be at a certain level of maturity before the structural mass, stiffness and damping properties can be available for a useful shimmy analysis[4,5].

Much work has been undertaken in the use of bifurcation analysis methods to determine the stability bounds of non-

linear systems in an efficient manner. Such techniques can be used to determine the effects of different parameters and characterise the types of nonlinear behaviour, including Hopf Bifurcations and period-doubling, etc. A key benefit of using such an analysis is that there is no need to result to the excessive blind Monte-Carlo simulations that are required when solely using numerical integration route. The AUTO software is well known as an approach to perform these computations[6]. Previous work has considered the use of this software on aircraft landing gears to detect stability bounds; however, this work only considered systems with relatively few degrees of freedom[7,8,9] . The coupling of multi-body undercarriage modelling with a bifurcation analysis package would enable the prediction of the onset of shimmy on full-size aircraft models in a rapid manner, which could be combined for parametric design, sensitivity and uncertainty studies.

Other work has considered the use of Singular Value Decomposition (SVD)[10,11,12] based approaches to produce reduced order models (ROMs) of aircraft models subjected to a wide range of different loading cases. It was demonstrated how these ROMs could be used to accurately and efficiently determine the worst case deterministic 1D and 2D loads. A further extension of the methodology was to use the ROMs to compute the uncertainty bounds for parameter variations[22,13,14,15].

In this work, the AUTO continuation software is coupled with the LMS Virtual.Lab Motion (VLM) multi-body software[16], to enable a bifurcation analysis to be applied to a representative non-linear multi-body nose landing gear structure. The approach uses the Singular Value Decomposition based techniques to compute the stability bounds (e.g. the onset of shimmy) in an efficient manner. Sensitivity[17,18] and uncertainty analyses are also performed to determine the influence of various structural parameters on the onset shimmy speed. Section II. describes the landing gear and tyre model. Section III., IV. and V. explain the methodology used to couple AUTO and LMS VLM, and perform the sensitivity and uncertainty analysis. Finally, Section VI. presents the results and demonstrates a comparison of the methodology with full-scale Monte-Carlo time simulations.

II. Landing Gear and Tyre Model

The landing gear model is a dual-wheel multi-body landing model in LMS Virtual.Lab Motion (Figure 1). The total number of generalized coordinates is 66, but, since the presence of 60 constraints, the degree of freedoms are six. In order to couple AUTO to LMS Virtual.Lab Motion the all states of the model are re-built at each step of the continuation based on the connectivity between the different bodies in the system[19]. In the developed code for coupling AUTO to LMS Virtual.Lab Motion, the six states considered for the continuation, as illustrated in Figure 1b, are:

- the rotation at the revolute joint between the main fitting and the fuselage; i.e. the lateral degree of freedom δ and the time-derivative $\dot{\delta}$. This DoF can be seen as a rotation about a point at a distance l_δ from the axle.

- the rotation at the revolute joint between the trail body and the main fitting; i.e. the torsional degree of freedom ψ and the time-derivative $\dot{\psi}$.

- the rotation at the revolute joint between the wheel axle and the trail body; i.e. the lateral degree of freedom Δ and the time-derivative $\dot{\Delta}$.

Another state that can be considered when modelling the tyre/ground interaction is the longitudinal rotation β of the landing gear (Figure 1c). This DoF can be seen as a rotation about a point at a distance l_β from the axle; however, β and its derivatives are always negligible in the computed analyses and in the present paper have not been considered to perform the continuation. This is motivated by the considered bracket joint that prevents all relative motion (translation and rotation), but the translation along the z-axis, between the fuselage and the ground. The translation along the x-axis is also constrained since, in order to perform continuation in terms of the forward velocity, the velocity is applied to the runway. In such a way, even applying a longitudinal force, the system is supposed to be in equilibrium at the velocity fixed during the bifurcation analysis, i.e. the presence of a control in terms of the forward velocity is assumed to be present.

The nominal values adopted for the structural parameters are provided in Table 1. It is worth to mention that the adopted values for both the landing gear and tyre model are not intended to represent any specific aircraft.

The transient tyre model is based on the formulation provided by Pacejka[20] for a single contact point transient tyre model (Figure 2). For each wheel two first order differential equations are adopted to model the contact patch lateral and longitudinal slip. Then the contact patch slip quantities are adopted as input for the steady-state tyre slip model to obtain as output the transient force and moment variation that act upon the contact patch[20]. The *Magic Formula* is the considered steady-state tyre model. Labelling with v_{α_i} and u_i the lateral and longitudinal tyre deflection and with α_i and k_i the lateral and longitudinal slip for the ith wheel, the contact patch slip quantities are modelled as it follows.

$$\frac{dv_{\alpha_i}}{dt} + \frac{1}{\sigma_{\alpha_i}} |V_{x_i}| \, v_{\alpha_i} = |V_{x_i}| \, \alpha_i = -V_{sy_i} \tag{1}$$

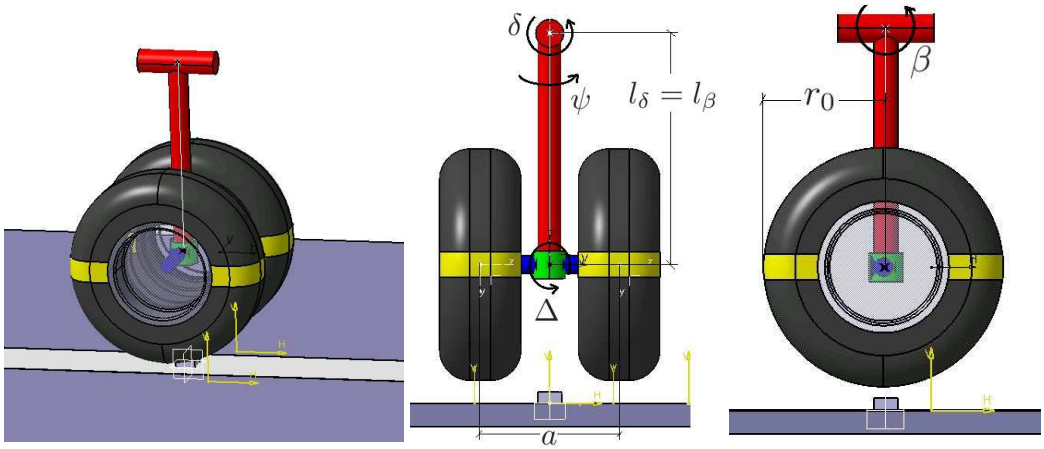

(a) (b) (c)

Figure 1: (1a)Adopted multi-body landing gear model in LMS Virtual.Lab Motion. (1b)Torsional (ψ) and lateral (δ and Δ) degrees of freedom. (1c) Longitudinal (β) degree of freedom.

$$\frac{du_i}{dt} + \frac{1}{\sigma_k}\,|V_{x_i}|\,u_i = |V_{x_i}|\,k_i = -V_{sx_i} \tag{2}$$

$$\tan\alpha_i = \frac{v_{\alpha_i}}{\sigma_{\alpha_i}} \qquad k_i = \frac{u_i}{\sigma_{\alpha_i}} \tag{3}$$

where

$$V_{sy_i} = V_{cy_i} \qquad V_{sx_i} = V_{cx_i} - \Omega_i \cdot r_0 \qquad V_{cx_i} \approx V_{x_i} \tag{4}$$

V_{x_i} and V_{cx_i} are the wheel centre longitudinal velocity and the longitudinal velocity of the contact centre C; V_{sx_i} and V_{sy_i} are the longitudinal and lateral wheel slip speeds of a point S attached to rim (Figure 2). σ_{α_i} and σ_k are the relaxation lengths adopted for the lateral and longitudinal slips, respectively. In the adopted model, the relaxation length of the lateral slip varies as the load acting on the wheel changes in order to replicate the physics as much as possible. The variation has been modeled relating σ_{α_i} with the contact patch h_i, whose change is mainly due to the loaded radius r_{1_i}, i.e. by the load experienced by the wheel[21]. The mathematical expression is given by

$$\sigma_{\alpha_i} = 3/2h \qquad h_i = r_0 \cdot 4 \cdot 0.85 \cdot \sqrt{(r_0 - r_{1_i})/(2 \cdot r_0) - ((r_0 - r_{1_i})/(2 \cdot r_0))^2} \tag{5}$$

Where r_0 is the unloaded radius. The coefficient that multiplies the contact patch h $(3/2)$ has been selected as suggested by the analysis performed by Besselink[8]. The longitudinal relaxation length has been kept fixed and equal to 0.4492.

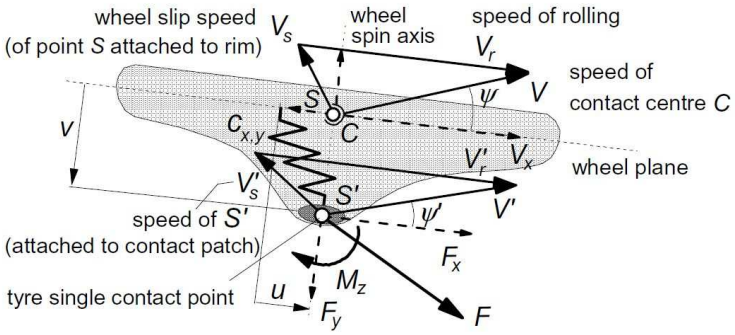

Figure 2: Single contact point tyre model showing lateral and longitudinal deflections[20].

Regarding the generalized forces due to the tyre/ground interaction, the expressions for the generalized forces in the *Magic Formula* formulation, but the normal load F_{z_i} is given by

$$\mathrm{D}\sin\left[\mathrm{C}\arctan(\mathrm{B}\xi - \mathrm{E}\,(\mathrm{B}\,\xi - \arctan\,(\mathrm{B}\xi)))\right] + \mathrm{S} \tag{6}$$

Parameter	Label	Nominal Value	Units
Unloaded radius	r_0	0.5	m
Gear length	l_δ	1	m
Mass of the fuselage	M_F	11000	Kg
Mass of the main fitting	M_{MF}	60	Kg
Mass of the wheel axle	M_{WA}	100	Kg
Mass of the wheel (left and right)	M_W	110	Kg
Stiffness fuselage - main fitting	k_1	$1.5 \cdot 10^6$	N m rad^{-1}
Stiffness main fitting - trail body	k_2	25000	N m rad^{-1}
Stiffness trail body - wheel axle	k_3	750000	N m rad^{-1}
Damping fuselage - main fitting of the left wheel	d_1	400	N m s rad^{-1}
Damping main fitting - trail body	d_2	400	N m s rad^{-1}
Damping trail body - wheel axle	d_3	400	N m s rad^{-1}
Inertia x (and y) axis - main fitting	$I1_{MF}$	0.164	kg m^2
Inertia z axis - main fitting	$I3_{MF}$	$6.136 \cdot 10^{-4}$	kg m^2
Inertia x (and y) axis - wheel axle	$I1_{WA}$	0.013	kg m^2
Inertia z axis - wheel axle	$I3_{WA}$	$4.771 \cdot 10^{-5}$	kg m^2
Inertia x (and z) axis - wheel (right and left)	$I1_W$	7	kg m^2
Inertia y axis - wheel (right and left)	$I2_W$	11	kg m^2

Table 1: Parameters and the range of values adopted in the Sensitivity Analysis

The specialization of the expression in eq. (7) depends on the analysed generalized force and if the considered tyre slip is pure longitudinal/lateral or the combination of them. The adopted expressions for the generalized forces acting on the wheels and the values of the coefficients used in the formulation are given in Appendix.

Figure 3 presents the sign - convention here adopted. In case of a pure side slip, the generalized forces present the following signs for positive a α_i and less than 14 deg

$$F_y(-) \qquad M_z(+) \qquad M_x(-) \tag{7}$$

For α_i greater than 14 deg the moment $M_z(+)$ presents a change in the sign.

For the present analysis assumptions are considered in order to have meaningful results using the tyre model for a nose landing gear. Change of the values of the coefficients that Pacejka[20] provides dealing with automotive system dealing with automotive system have been made also simulating the same landing gear-tyre model with the velocity applied to the fuselage and allowing the translation of the fuselage along the x-axis to be free of any constraints. In particular:

– q_{Sx3}, a coefficient used in the modeling of the overturning couple (Appendix), has been selected different from zero in order to take into account the moment generated for the variation of the centre of pressure of the lateral force F_{yi} due to a lateral slip. The values of X_L and q_{Sy2}, coefficients used in the modeling of lateral force and

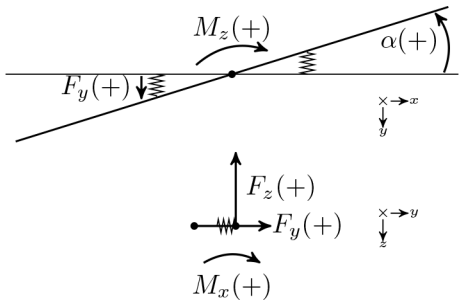

Figure 3: Sign-convetion here adopted

rolling resistance moment respectively (Appendix), have been selected so that a stable solution occurs at low velocity.

– all the residual terms that cause generalized forces different than zero in presence of zero lateral/longitudinal slip are neglected. In fact, for a symmetric nose landing gear system, in presence of a symmetric maneuver, have not reason to be considered.

– the variation of the centre of pressure of the forces is considered by the introduced moments. However, since in VLM the forces have been applied at the centre of the wheels, additional moments have to be considered. The total moment is thus given by

$$\mathbf{M_{tot}} = \begin{bmatrix} Mx \\ My \\ Mz \end{bmatrix} - \begin{bmatrix} 0 \\ 0 \\ r_{1_i} \end{bmatrix} \times \begin{bmatrix} F_x \\ F_y \\ 0 \end{bmatrix} \tag{8}$$

Where M_z, F_x and F_y are fixed equal to M_{z_0}, F_{x_0} and F_{y_0} if the pure slip is considered.

Thanks to such a formulation it is possible to perform a bifurcation analysis considering the effects due to lateral slip as well as longitudinal slip and to gyroscopic effects.

III. Methodologies

In the present section the methodologies developed to perform bifurcation analysis of a nonlinear multi-body system are briefly sketched out.

A. AUTO - LMS Virtual.Lab Motion coupling

Figure 4 presents the developed coupling between AUTO and LMS Virtual.Lab in a Matlab/Simulink environment. The integration of the system of equations characterizing the analyzed system is performed through co-simulation. In particular the block labelled as plantout-function in Figure 4 is the one related to the multi-body system in VLM. Regarding the continuation, the selected continuation parameters are the forward velocity V and the vertical load experienced by the nose landing gear $\overline{W}_n$, namely the actual weight on the nose landing gear minus the lift that decreases the total weight of the aircraft for non zero forward velocity. These are control outputs for Simulink and control inputs for the VLM multi-body model, which is solved, as stated, in co-simulation with Matlab. In LMS Virtual.Lab Motion it is possible to define which are the inputs and outputs of interest in the simulation. In order to perform the continuation it is necessary to define the differential equations of interest. Using AUTO, the differential equations of interest can also be considered in the absence of an analytical equation, and defined by specifying the values of the derivatives and the states in the Matalb/Simulink environment. In order to couple AUTO with LMS Virtual.Lab Motion, the set of joint states (δ, $\dot{\delta}$, ψ, $\dot{\psi}$, Δ, $\dot{\Delta}$) has been selected. Thus, the functions of interest for the continuation are defined between the values of the derivatives of the mentioned states and the values acquired by the states at each analysed continuation step. Finally, the developed solution adopts an external tyre model for which the transient tyre/ground interaction has been modelled (section II.). Also the adopted tyre states have to be considered to perform the continuation. For instance, if only the lateral slip is considered for each tyre, then there are $6 + 2$ states considered in the continuation; if both the lateral and longitudinal slips are taken into account, then there are $6 + 4$ states. In the Matlab/Simulink environment the continuation parameters and the states of the model are changed during the continuation in order to identify the equilibrium solutions. The forces due to the ground-tyre interaction are then generated always in the Matlab/Simulink environment, coherently to the values assumed by the continuation parameters and the states of the landing gear model, and . In order to perform the bifurcation analysis,

first the equilibrium solution has to be identified as the forward velocity V varies. Then, the bifurcation analysis can be performed in more parameters and continuing other possible branches that start from possible bifurcation points.

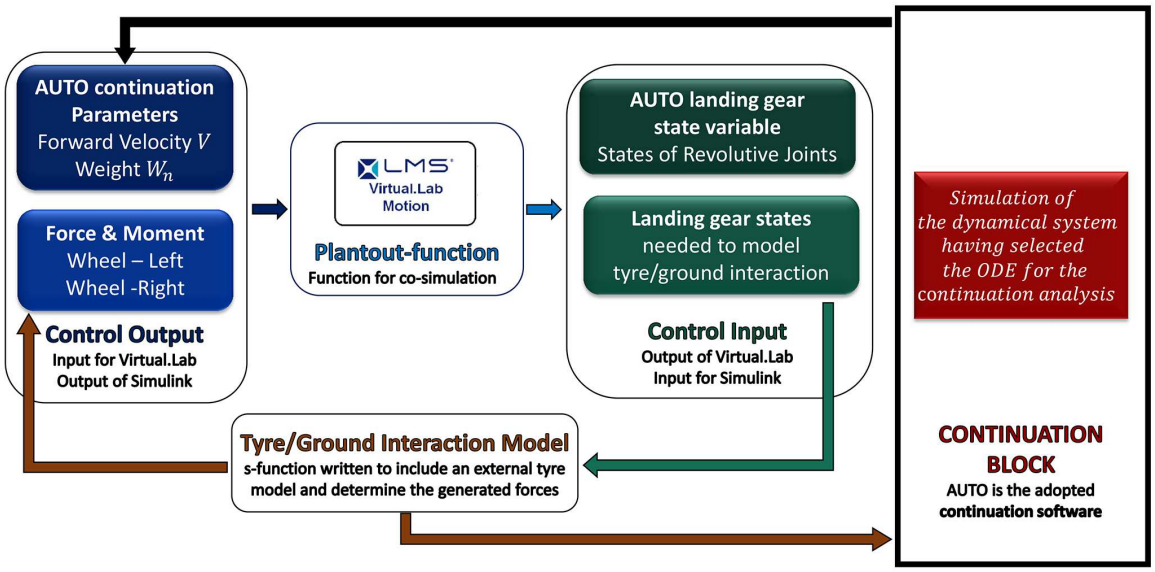

Figure 4: Developed solution to couple AUTO to LMS Virtual.Lab Motion.

B. Sensitivity Analysis and Uncertainty Quantification

?? The identification and description of the locus of Hopf bifurcation points in presence of uncertainty is not trivial and the developed technique apply bifurcation analysis to a multi-body system is presented in figure 5. The main steps are:

1. Define the sampling planes to train and validate the surrogate models adopted to perform sensitivity analysis.
2. Perform a global sensitivity analysis in order to identify the most influential uncertain factors. In order to fulfill this step, two objective functions have been considered to capture a variation in the shape and a translation of the locus of Hopf bifurcation. The slope at equidistant points on the locus of Hopf bifurcation points in the $(\overline{W}_n, V)$ parameter space and the forward velocity V, characterizing the extreme point at the lower V for each locus of points, have been selected as the stated objective functions. The variation in the shape and/or translation of the locus of Hopf bifurcation is then discussed using the adopted main and total indices.
3. Define the sampling plane in terms of the most influential uncertain factors to perform the uncertainty quantification.
4. Perform the uncertainty quantification using the developed SVD/HOSVD based methodology and exploiting Blind Kriging metamodels[22].

In order to perform both the Sensitivity and Uncertainty analysis the locus of Hopf bifurcation points are discretized in a number $B+1$ of points. The first and last points of all the analysed locus of points are fixed to a same value of the vertical load experienced by the nose landing gear $\overline{W}_n$ (Figure 6) in order to start from the same value of the vertical load to perform the discretization.

IV. Sensitivity Analysis

SA has its origin in the design of experiments (DOE), which was introduced in order to evaluate the input/output (I/O) relation in the presence of variation in parameters. In the analysed problem, sensitivity metrics that capture non-linear dynamical behaviour and high order interaction are desirable and for this reason the *Sobol' indices*[17] and the total effect index S_{T_i} have been selected. These are parts of the *global* SA methods and are able to correlate the output variation with the variation in the parameters exploiting statistical means and usually adopting a sampling approach. A sensitivity method is said to be global if all parameters are simultaneously varied and the sensitivity is evaluated over the range of each parameter[18]. The *Sobol' indices* for the parameters $(x_1, x_2, ..., x_s)$ are given by

$$S_{i_1 \ldots i_s} = \frac{V_{i_1 \ldots i_s}}{V} \tag{9}$$

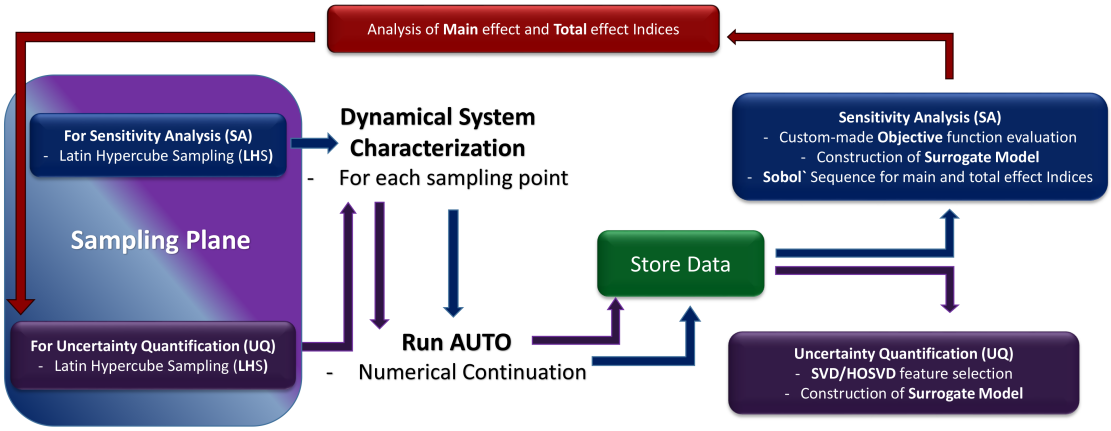

Figure 5: Developed methodology to perform sensitivity and uncertainty analysis in terms of bifurcation diagrams

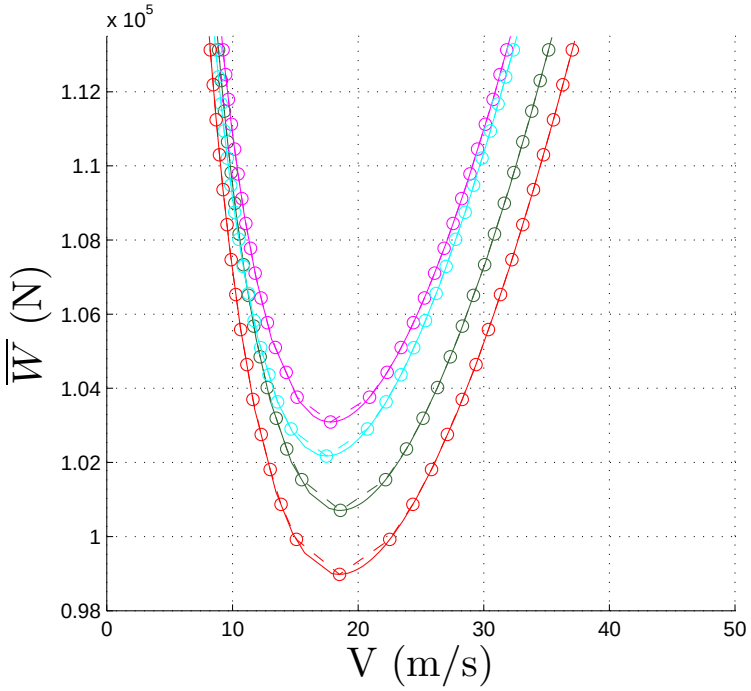

Figure 6: Adopted discretization of the locus of Hopf bifurcation points. For instance, four locus of Hopf bifurcation points obtained for four different set of parameter values are shown.

which are all non-negative leading to the result

$$\sum_{s=1}^{n} \sum_{i_i=1<\ldots<i_s}^{n} S_{i_1 \ldots i_s} = 1 \tag{10}$$

where V and $V_{i_1 \ldots i_s}$ are called total variance of a function of interest f and variance of f relative to the parameters $(x_1, x_2, ..., x_s)$. The reason for such terminology is due to the fact that they would actually be these variances if the parameters x were randomly *uniformly* distributed in the domain of interest.

Sobol' indices are extremely powerful and can be adopted for three different types of problems exploiting the fact that the higher the value of the index $S_{i_1 \ldots i_s}$, the more important are the parameters $(x_1, x_2, ..., x_s)$ and their integration. The three problems are:

1. ranking of variables
2. identifying non-essential variables
3. detecting high order members.

The selection of the parameters that the most influence a variation in the branches presented in subsection **??**, parameters that have to be then considered to perform UQ, is a problem that belongs to the points 1 and 2 above. The main effect S_i and total effect index S_{T_i}, introduced by Saltelli[18-23], have been considered. Saltelli has emphasized the importance of S_{T_i}, which measures the total effects (i.e. first and higher order interaction) of parameter x_i, especially in the presence of a large number of parameters. The sum of these indices $\sum_{i=1}^{n} S_{T_i}$ must be greater than or equal to 1. The equality occurs only in the case of a perfect additive model and in that case $\sum_{i=1}^{n} S_i = 1$.

The main effect S_i and total effect S_{T_i} are obtained as[24]

$$S_i = \frac{V_{X_i}(E_{\mathbf{X}_{\sim \mathbf{i}}}(Y|X_i))}{V(Y)} \tag{11a}$$

$$S_{T_i} = \frac{E_{\mathbf{X}_{\sim \mathbf{i}}}(V_{X_i}(Y|\mathbf{X}_{\sim \mathbf{i}}))}{V(Y)} = 1 - \frac{V_{\mathbf{X}_{\sim \mathbf{i}}}(E_{X_i}(Y|\mathbf{X}_{\sim \mathbf{i}}))}{V(Y)} \tag{11b}$$

where Y is the function of interest f, $E_X(\cdot)$ and $V_X(\cdot)$ are the mean and variance of argument $(\cdot)$ over $\mathbf{X_i}$, while $E_{\mathbf{X}_{\sim \mathbf{i}}}(\cdot)$ and $V_{\mathbf{X}_{\sim \mathbf{i}}}(\cdot)$ are the mean and variance of all parameters X but X_i.

In order to efficiently perform the SA, a computational approach that allows a simultaneous computation of S_i and S_{T_i} has been adopted and the indices are evaluated using a surrogate model (Blind Kriging) developed for each selected output u, trained and validated with a suitable number of sampling points, adopting Sobol' sequences (also known as LP_τ sequences) as the quasi-Monte Carlo algorithms. An analytical evaluation of such indices is feasible just for simple systems, which is not the case here. The considered numerical computation has been presented by Saltelli[24,25] and consists of using two independent $N \times k$ matrices $\mathbf{A}$ and $\mathbf{B}$, whose rows and columns are the considered sampling points and design variables respectively, and a third $(N \cdot k) \times k$ matrix $\mathbf{C}$ that is constructed from the previous ones. Each $\mathbf{C^{(i)}}$ block ($i = 1...k$) of the matrix $\mathbf{C}$ can be formed:

1. by all columns of $\mathbf{A}$ except the $i-th$ column, which is taken by $\mathbf{B}$
2. by all columns of $\mathbf{B}$ except the $i-th$ column, which is taken by $\mathbf{A}$

Whatever case is chosen, $N \times (k+2)$ model evaluations are required to determine the sought indices. Saltelli[24] showed that with the first algorithm a higher rate of convergence is achieved if the following formula for $V_{X_i}(E_{\mathbf{X}_{\sim \mathbf{i}}}(Y|X_i))$ and $E_{\mathbf{X}_{\sim \mathbf{i}}}(V_{X_i}(Y|\mathbf{X}_{\sim \mathbf{i}}))$ are adopted to calculate S_i and S_{T_i}, respectively:

$$V_{X_i}(E_{\mathbf{X}_{\sim \mathbf{i}}}(Y|X_i) = \frac{1}{N}\sum_{j=1}^{N} f(\mathbf{B})_j \left(f\left(\mathbf{C^{(i)}}\right)_j - f(\mathbf{A})_j \right) \tag{12a}$$

$$E_{\mathbf{X}_{\sim \mathbf{i}}}(V_{X_i}(Y|\mathbf{X}_{\sim \mathbf{i}})) = \frac{1}{2N}\sum_{j=1}^{N} \left(f(\mathbf{A_j}) - f\left(\mathbf{C^{(i)}}\right)_j \right)^2 \tag{12b}$$

The last term to be calculated is the total variance V and, since it is a function of f_0^2(f_0 is the mean effect of the function of interest f), a formula for f_0 is also required. The existence of three possible equations for V and four for f_0 have been found[26], giving a total of 12 possible combinations such that:

$$\hat{f}_0^2 = \left(\frac{1}{N}\sum_{j=1}^{N} f(\mathbf{A}) \right)^2 \tag{13a}$$

$$\hat{f}_0^2 = \left(\frac{1}{N}\sum_{j=1}^{N} f(\mathbf{B}) \right)^2 \tag{13b}$$

$$\hat{f}_0^2 = \left(\frac{1}{2N}\sum_{j=1}^{N} f(\mathbf{A},\mathbf{B}) \right)^2 \tag{13c}$$

$$\hat{f}_0^2 = \frac{1}{N}\sum_{j=1}^{N} f(\mathbf{A}) f(\mathbf{B}) \tag{13d}$$

$$\hat{V} = \frac{1}{N-1}\sum_{j=1}^{N} f^2(\mathbf{A}) - \hat{f}_0^2 \tag{14a}$$

$$\hat{V} = \frac{1}{N-1}\sum_{j=1}^{N} f^2(\mathbf{B}) - \hat{f}_0^2 \tag{14b}$$

$$\hat{V} = \frac{1}{2(N-1)}\sum_{j=1}^{2N} f^2(\mathbf{A},\mathbf{B}) - \hat{f}_0^2 \tag{14c}$$

In the present analysis, all of these combinations have been considered and compared in order to find the one that gives the most coherent result with respect to the stated properties of the indices and with the lowest computation time for convergence.

Sobol' indices can be evaluated using surrogate models of the selected outputs u, trained with a suitable number of sampling points[‖]. These surrogate models are related to $(B+1)$ points on each first set of identified branch, one for all the considered sampling points. These points are obtained by dividing each identified branch in an equal number of intervals B.

In order to consider the importance of the design parameters, and so determine the Sobol' indices, it is important to select suitable objective functions u, for use with the Sobol' indices. For the landing gear system the objective functions u have been defined having fixed the two parameters that are considered as operating ones due to their importance for a landing gear system: the forward velocity V and the vertical force on the landing gear $(\overline{W}_n, V)$. The qualitative change in the branches can be captured if the objective functions describe both variation in the **shape** and **translation** of the interesting branches. Thus, two kinds of indices have been selected:

1. for each determined segment on the analysed branches, the approximated slope is taken as an objective function to capture change in the **shape** of the analysed branch as parameters $\mathbf{p}$ change

$$f_{1b_{i_1\ldots i_s}}(p_{i_1\ldots i_s}) = \left.\frac{\partial F_z}{\partial V}(p_{i_1\ldots i_s})\right|_b \simeq \left.\frac{\Delta F_z}{\Delta V}(p_{i_1\ldots i_s})\right|_b \qquad b = 1\ldots B \quad 1 \le i_1 < \ldots < i_s \le N_P \tag{15}$$

2. at the first determined Hopf bifurcation point, i.e. at which the continuation has been switched in two parameters, the velocity V_1 is considered as an objective function to discuss **translations** of the interesting branch

$$f_{2_{i_1\ldots i_s}}(p_{i_1\ldots i_s}) = V_1(p_{i_1\ldots i_s}) \qquad 1 \le i_1 < \ldots < i_s \le N_P \tag{16}$$

where N_P is the number of the analysed parameters. Thus, in total $(B+1)$ objective functions are considered and the first B have to be considered as a whole since since they describe the change in the **shape** of the interesting branch; the mean in terms of all the intervals B has been considered for each branch. If a significant topology variation of the bifurcation diagram occurs changing a particular parameter, then this should be considered as an operating parameter.

Once the SA is accomplished, then the UQ can be performed in terms of the most influential uncertain parameters. In the following subsection the adopted new methodology is presented. It is based upon the same principles characterizing the already tested technique developed by the authors to predict and propagate parametric uncertainties up to correlated time-history quantities[22].

V. Uncertainty Quantification

The Uncertainty Quantification has been performed using a speed up process already implemented by the authors to propagate uncertainty in terms of correlated aircraft loads[22,13] and shimmy phenomena for a simplified analytic landing gear model[14]. The speed up process has been developed using the Singular Value/High Order Singular Value Decomposition (SVD/HOSVD) and surrogate modelling technique. Then, a geometric based approach has been developed to determine the outer bounds for the occurrence of shimmy and probabilistic described the occurrence of Hopf bifurcation points in the $(\overline{W}_n, V)$ parameter space.

The SVD/HOSVD is here considered for feature extraction. In particular, the terms to be retained in order to speed up the process are identified fixing the maximum acceptable error caused by the rank reduction. Once this error is chosen, the energy 'captured' by the reduced matrix/tensor (captured energy criterion[27]) and the singular values to be retained can be identified. The stated energy is linked with the Frobenius norm and is adopted by the captured energy criterion to identify the rank reduction. The new method overcomes the difficulties in identifying the best rank reduction using the SVD/HOSVD. Indeed the energy criterion faces the issue just mathematically and the physics of the analyzed problem is lost. The captured energy criterion consists of selecting enough singular values of the matrix of interest, the unfolding matrix $\mathbf{A}_{(\mathbf{1})}$ for the considered HOSVD[15], such that the sum of their squares is a certain percentage T of the total sum of the squared values. The reason for such a decision is that the resulting

[‖] Blind Kriging surrogate models have been adopted.

matrix 'captures' $T\%$ of the Frobenius norm of the full matrix, that is correlated with the energy. In the method here proposed, the singular values (surrogate models) characterizing the SVD or the HOSVD are automatically obtained once the stated maximum acceptable error is defined; moreover, the percentage $T\%$ can be also obtained to proof that the threshold one should consider for $ST\%$ is not absolute and often difficult to be known a priori. The authors have considered an iterative procedure, the number of singular values is increased, and so the percentage $T\%$, and the rank reduction coherently updated until the desired maximum error is met. Finally, regarding the error metric, the Mean Average Percentage Error (MAPE) is here considered and the average is in terms of all the considered training points.

Regarding the geometric based method, Figure 7 presents the steps that need to be followed. 7

1. the lower and upper bounds of the locus of Hopf bifurcation points are identified and discretized in an equal number of points, the corresponding points are index with the same number.

2. directions of interest are defined as the line connecting the points with the same index and at the lower and upper bound.

3. the SVD/HOSVD based method[22 13 14] is then considered to determine locus of Hopf bifurcation for an arbitrary number of points in the sampling plane defined in terms of the uncertain parameters. Thus, considering the intersection of the determined locus of Hopf bifurcation with the direction of interest, a probabilistic description in terms of the locus of Hopf bifurcation points can be drawn.

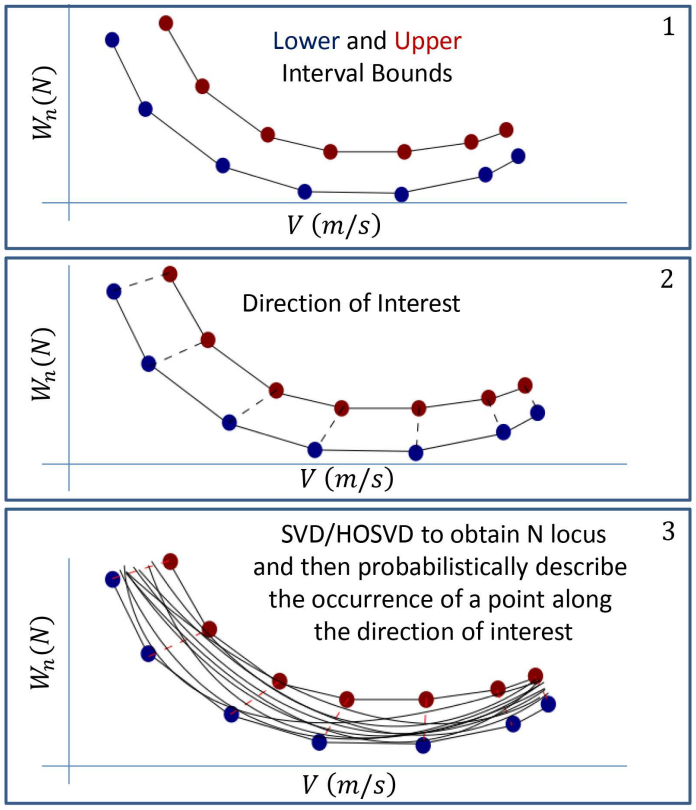

Figure 7: Steps to be followed to apply the geometrical based method.

After having evaluated N locus of Hopf bifurcation points using the SVD/HOSVD based method, first the worst lower and upper bounds for the locus of Hopf bifurcation points are determined and discretized in the selected $B+1$ number of points. Thus, the directions of interest are identified by the couple of points at the lower and upper bounds at the same index of discretization. Eventually, the intersections between the N generated locus of Hopf bifurcation and each of the defined directions of interest are determined. Thus, the distances between the intersecting points and the points on the lower bound at the correspondent index are determined. A probabilistic description of the distance at each direction of interest can be then be determined and locus of Hopf bifurcation points for a same quantile value can be identified.

VI. Results

In this section, first the results of the validation of the developed code to couple Virtual.Lab motion with AUTO and the sensitivity analysis are provided. Then the validation of the surrogate models adopted in the SVD/HOSVD based method and the output given by the uncertainty propagation will be presented.

A. Landing Gear Bifurcation Analysis using VLM-AUTO coupling

Very good results have been obtained performing bifurcation analysis using the nonlinear multi-body landing gear model considering an external tyre model for each wheel representing the effects due to lateral slip and combining side and longitudinal slip. The tyre/ground interaction has been modeled adopting the approach presented in section II.. The results presented in this subsection are referred to the landing gear model whose structural parameters have the nominal values provided in Table 1 (section II.).

The bifurcation analysis has been adopted to identify first points of Hopf bifurcation as the forward velocity V changes and then the locus of these points in the $(\overline{W}_n, V)$ parameter space.

The rotation of the wheels (and so gyroscopic effects) has been included in the analysis. However, it is worth to mention that it reduces the range of forward speed for which the shimmy phenomenon occurs, but increasing the range of vertical load experienced by the nose landing gear $(\overline{W}_n, V)$. This is shown in Figure 8, unstable equilibrium solutions characterize the all the points in the convex region and here LCOs (shimmy phenomena) occur.

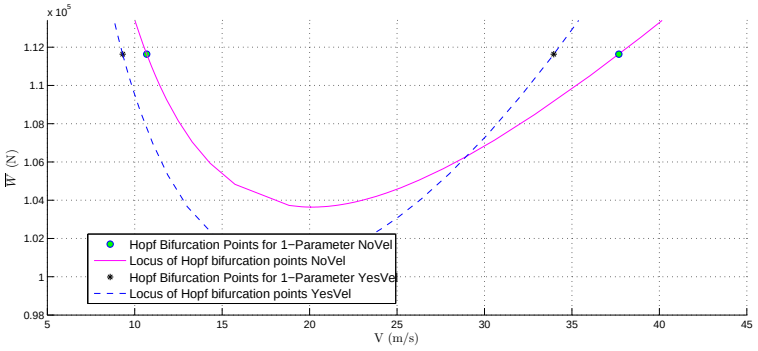

Figure 8: Comparison of two parameter bifurcation diagrams, namely the locus of Hopf bifurcations in the $(\overline{W}_n, V)$ parameter space, considering (YesVel) or not (NoVel) the wheels rotating, obtained coupling AUTO with LMS Virtual.Lab Motion.

The linear stability of the analyzed system is summarized using the root locus in Figure 9. Here the eigenvalues of the system in which a pure side slip or the combined slip is considered are represented as the velocity changes. The range of the considered velocity is [0,100] m/s. It is apparent that there are two complex eigenvalues for which the stability is lost, in particular this happens at 10.3 m/s and 11.18 m/s for the system in which the side and combined slip is considered, respectively. Then, respectively at 31.92 m/s and 25.13 m/s, the stability is reacquired. As it will be shown in the results obtained performing bifurcation analysis, Hopf bifurcations occur at such a points.

Figure 10 shows the comparison of one parameter bifurcation diagrams as the forward velocity V changes obtained including the dynamics of a pure side or combined slip for the wheels. The diagrams are in terms of the states of the landing gear model adopted to perform the continuation. With respect to the tyre model - states, if a pure side or combined slip is included in the model, the side slip of the left and right wheels (λ_L and λ_R) is considered. Two Hopf bifurcations occur at 10.3 m/s and 31.92 m/s or at 11.18 m/s and 25.13 m/s if a pure side slip or a combined slip condition is considered. The shimmy phenomenon is primarily related to the lateral dynamics in both the analyzed conditions: the lateral state δ is the one that presents the highest amplitude. In terms of one parameter bifurcation diagrams, there is a difference between the two analyzed conditions; if a combined slip condition is considered a reduction in terms of the amplitude occurs. Moreover, the range of velocity for which shimmy occurs is smaller if the longitudinal slip is considered. However, the LCO is always stable as the velocity varies in both the analyzed conditions.

Figure 11 presents the comparison of the bifurcation diagram in two parameters obtained including the dynamics for a pure or combined slip in the tyre model. As previously stated, unstable equilibrium solutions characterize the all the points in the convex region and here LCOs (shimmy phenomena) occur. The considered parameters are the forward velocity V and the vertical load experienced by the nose landing gear $\overline{W}_n$. The determined branch presents a trend that is physically meaningful: decreasing the load $\overline{W}_n$ causes the interaction between the tyre dynamics and the landing gear to decrease. Thus, the range of the forward velocity V in which the LCO can occur reduces as $\overline{W}_n$ decreases and eventually no Hopf bifurcations occur. Moreover, the higher the $\overline{W}_n$, the lower the velocity for which

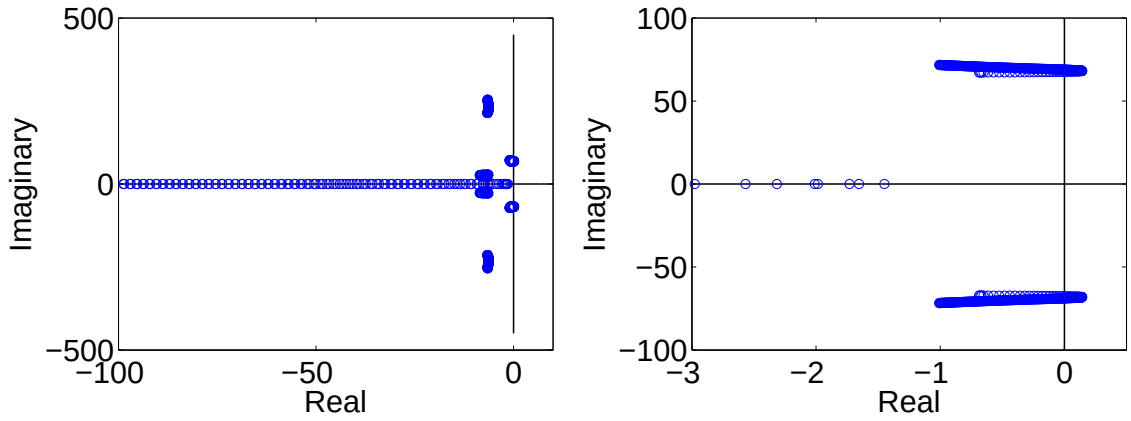

(a) Pure Slip. On the right size the root locus is zoomed in.

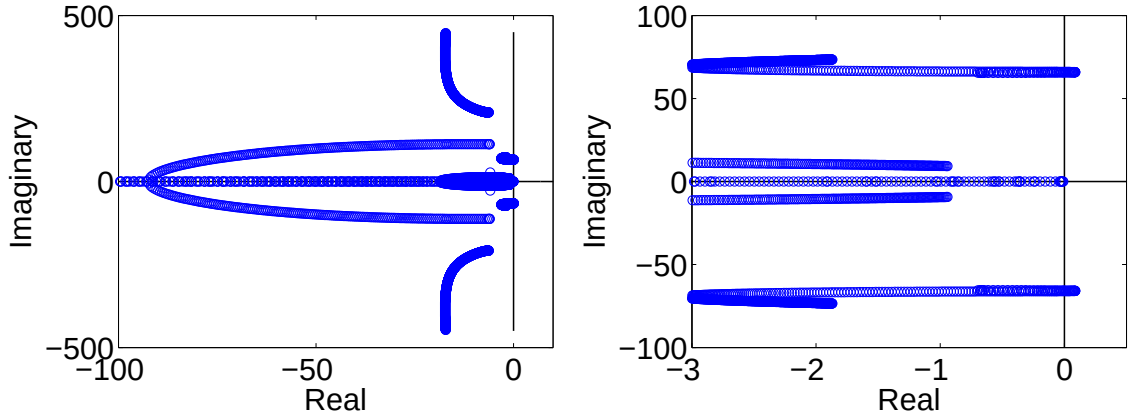

(b) Combined Slip. On the right size the root locus is zoomed in.

Figure 9: Root Locus characterizing the analysed landing gear+tyre model as the velocity changes.

a first Hopf bifurcation occurs. Comparing the results obtained including or not the longitudinal slip, it can be noticed that the shimmy phenomenon occurs for a smaller range of velocity V (as discussed dealing with the one parameters bifurcation diagrams) and vertical load experienced by the nose landing gear $\overline{W}_n$. In order to emphasize the accuracy of the results obtained adopting the developed code for coupling LMS Virtual.Lab Motion to AUTO, Table 2 shows the percentage differences for a stable periodic solution identified through continuation, namely using the developed code to couple AUTO to LMS Virtual Lab Motion (VLM). The comparison is performed in terms of the maximum values and the period obtained using the bifurcation analysis and simulating directly the multi-body model in LMS Virtual.Lab Motion giving as initial conditions those related to the point on the periodic branch for a velocity V equal to 17 m/s.

Figure 12, 13 and 14 show the spectrum of the time history of the states of the landing gear and tyre. Figure 12 and 13 present the comparison between the two slip conditions, the blue and the green lines are for the pure and combined slips, respectively. The lateral shimmy phenomenon is not changed including the longitudinal slip in the present analysis. The shimmy phenomenon shows the same frequency in AUTO and VLM for both pure lateral and combined slip. As presented in Figures 12, 13 and 14 the main frequency content is at 11 Hz; however frequency content at multiples 11 Hz are also present, but for lower amplitude. The states ψ and Δ present terms different from zero at 33 Hz, λ_L and λ_R very low content at 22 Hz and u_L and u_R presents terms at 22, 33, 44 and 55 Hz. The longitudinal side slip states presents also a component different from zero at 0 Hz and this means that the time history is periodic but around a value that is not zero but with an amplitude equal to $5 \cdot 10^4$. For the sake of completeness, Figures A. A. A. show the phase plots in terms of states δ, ψ, Δ, λ_i and u_i obtained using the multi-body landing gear model, for which the dynamics for both the lateral and longitudinal slips are included. These are obtained giving as initial conditions those characterizing the point on the periodic branch (Figure 10) for $V = 17$ m/s. These figures reflect the frequency content and the fact that a limit cycle is actually occurring. The phase plots are closed curves because the frequency characterizing the evolution of the states are all multiples one each other and this happens for instance in the Lissajous curves (N. Bowditch and J. A. Lissajous).

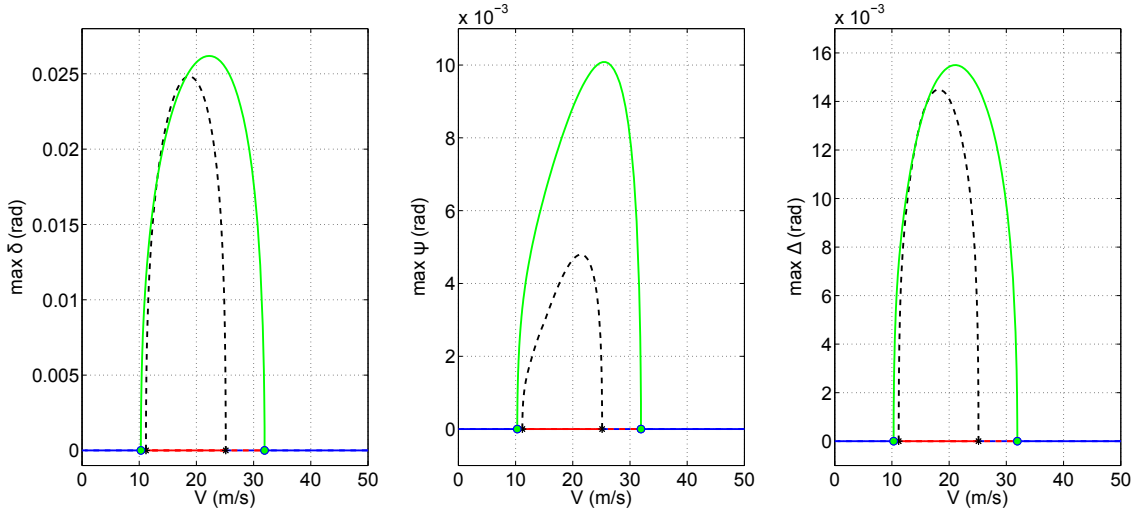

(a) Rotation states at the joints.

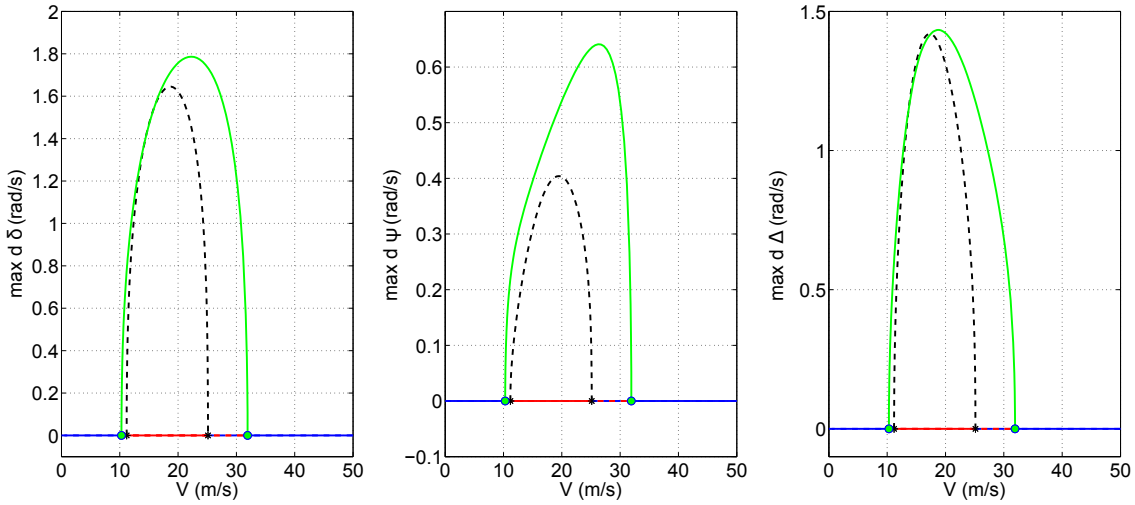

(b) Derivative of rotation states at the joints.

Figure 10: One parameter bifurcation diagrams obtained coupling AUTO with LMS Virtual.Lab Motion. Periodic orbits are shown as maximum amplitude. The blue and red lines are used for stable and unstable equilibrium solutions. The green and dot black line are used for the periodic branches.

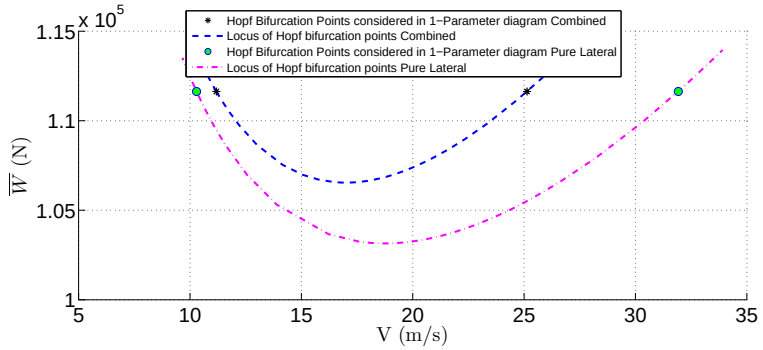

Figure 11: Comparison of two parameter bifurcation diagrams, namely the locus of Hopf bifurcations in the ($\overline{W}_n$,V) parameter space, obtained coupling AUTO with LMS Virtual.Lab Motion.

$V(m/s)$	State	Maximum Value			Period		
		AUTO-VLM (rad)	VLM (rad)	$\epsilon(\%)$	AUTO-VLM (s)	VLM (s)	$\epsilon(\%)$
17	δ	$2.4 \cdot 10^{-2}$	$2.33 \cdot 10^{-2}$	3	$9 \cdot 10^{-2}$	$9 \cdot 10^{-2}$	0
	ψ	$7.5 \cdot 10^{-3}$	$7 \cdot 10^{-3}$	7			
	Δ	$1.45 \cdot 10^{-2}$	$1.4 \cdot 10^{-2}$	3.5			

$V(m/s)$	State	Maximum Value			Period		
		AUTO-VLM (rad)	VLM (rad)	$\epsilon(\%)$	AUTO-VLM (s)	VLM (s)	$\epsilon(\%)$
17	δ	$2.5 \cdot 10^{-2}$	$2.64 \cdot 10^{-2}$	-5	$1.5 \cdot 10^{-1}$	$1.5 \cdot 10^{-1}$	0
	ψ	$4.6 \cdot 10^{-3}$	$5 \cdot 10^{-3}$	-8			
	Δ	$1.43 \cdot 10^{-2}$	$1.53 \cdot 10^{-2}$	-7			

Table 2: Comparison of the the maximum values of a periodic solution identified using the developed code to couple AUTO to LMS Virtual Lab Motion (VLM). The compared values are between those obtained with AUTO-VLM and those got by simulating the multi-body model in VLM giving as initial conditions the ones characterizing the selected point on the stable branch of periodic orbits. (Top for the tyre model in which the lateral slip is included; bottom for the tyre model in which both the slips are included.)

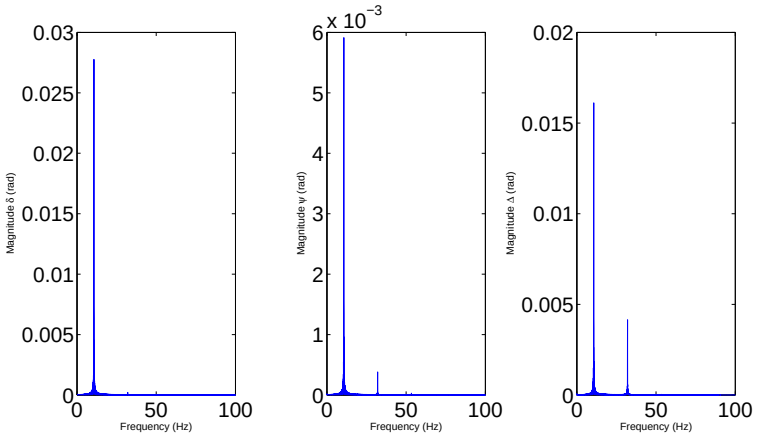

Figure 12: Frequency spectrum for the time history characterizing the evolution of landing gear states at the point on the the period branch for $V = 17$ m/s. The blue and the green lines are for the pure and combined slips.

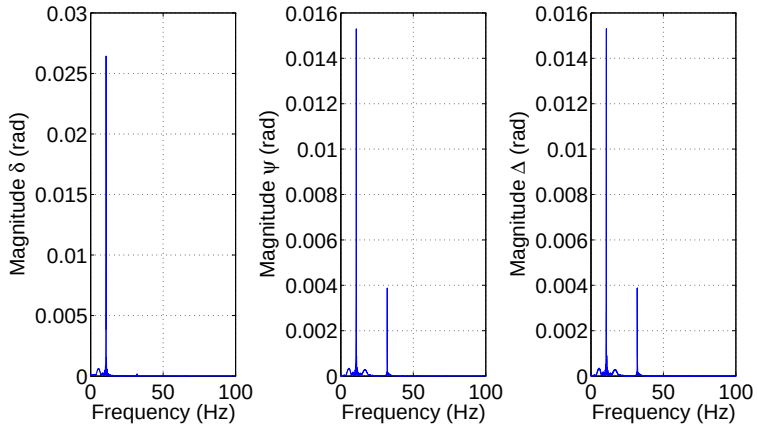

Figure 13: Frequency spectrum for the time history characterizing the evolution of side slip states at the point on the the period branch for $V = 17$ m/s. The blue and the green lines are for the pure and combined slips.

B. Sensitivity Analysis

In order to detect the parameter whose variations influence the most the shimmy occurrence, i.e. that change the most the locus of Hopf bifurcation points, a sensitivity analysis has been performed. The main and total effect indexes have been considered as specified in section IV.. In the same section, the selected objective functions are also presented.

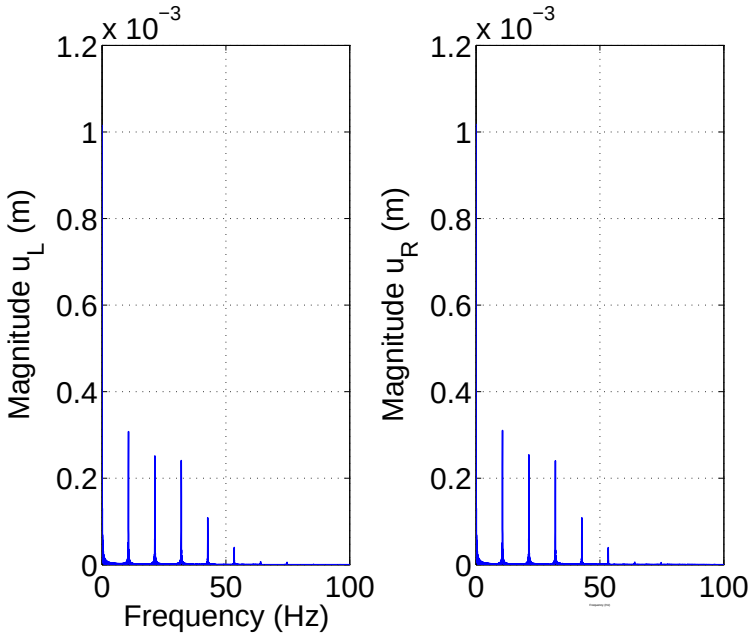

Figure 14: Frequency spectrum for the time history characterizing the evolution of longitudinal slip states at the point on the the period branch for $V = 17$ m/s.

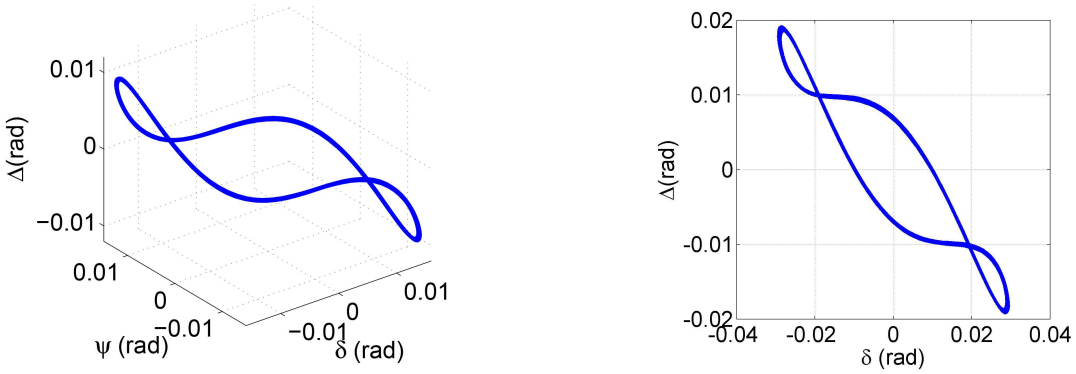

(a) Phase plots in terms of the states δ, ψ and Δ.

(b) Phase plots in terms of the states δ and Δ.

Figure 15: Phase plots of the states considered to perform the bifurcation analysis obtained at a point on the periodic branch for $V = 17$ m/s.

Regarding the parameters and the relative variations, 15 parameters have been considered and table 3 provides the names, the label and the relative adopted variation ($\pm 7\%$). Log-uniform and uniform probability distributions have been adopted if the variation of the analyzed parameter is greater or less of one order of magnitude, respectively. This choice is due to the lack of information about the parametric uncertainty [18].

The surrogate models considered to perform the sensitivity analysis are for the slopes at each of the B discretized point on the locus of hopf bifurcation (first objective functions) and for the the point at which the variation of the forward velocity as the parameters vary is analysed (second objective functions). The discretized points are 31 and the surrogate models are trained using 100 sampling points and have been validated considering 50 validation points. The $MAPE$ for both the analyzed conditions are shown in Table 4. It is apparent that the trained surrogate model replicates the actual objective functions with good accuracy.

Using the surrogate models, Saltelli's technique has been adopted to evaluate the main and total effect indices, and all the 12 combinations to determine the total variance V have been considered (section IV.). For the sake of clarity, these have been numbered as shown in Table 5. The blind kriging models have been adopted as surrogate models.

Different numbers of evaluations of the surrogate models have been considered to test the performance in terms of convergence of the different expressions to evaluate the main and total effect indices . The main and total effect indices of all the defined objective functions empathize that the best combination is either the 4^{th} or 8^{th} one, for which the indices converge to a constant value for a number of emulations greater than 4000. This result is shown here in

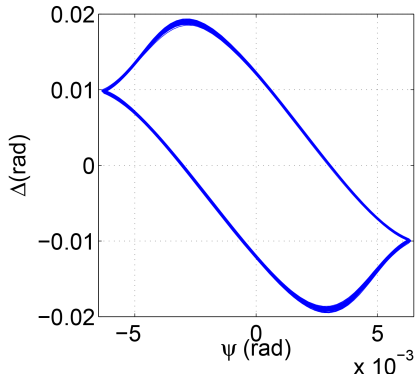

(a) Phase plots in terms of the states ψ and Δ.

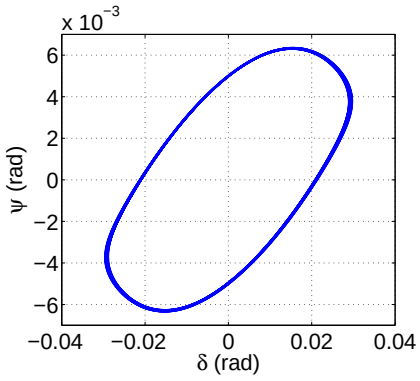

(b) Phase plots in terms of the states δ and ψ .

Figure 16: Phase plots of the states considered to perform the bifurcation analysis obtained at a point on the periodic branch for $V = 17$ m/s.

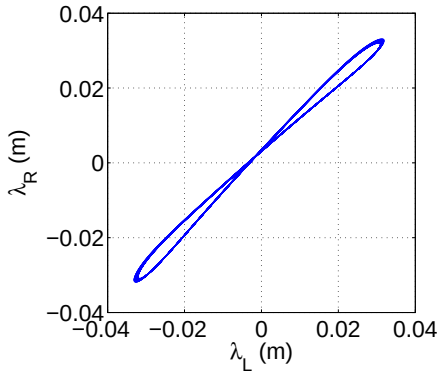

(a) Phase plots in terms of the states λ_L and λ_R.

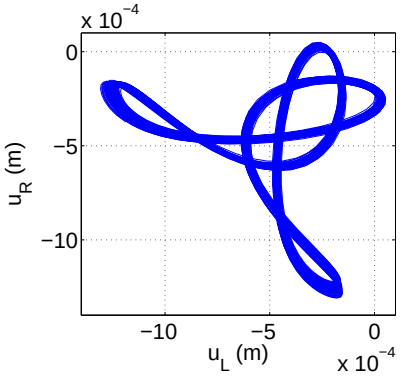

(b) Phase plots in terms of the states u_L and u_R.

Figure 17: Phase plots of the side and longitudinal slip states considered to perform the bifurcation analysis obtained at a point on the periodic branch for $V = 17$ m/s.

Figures 18 and 19, which provide for the sake of conciseness just the comparison for the sum of the main and total indices related to the 25^{th} slope. Looking at the 4^{th} or 8^{th} combinations, it can be noticed that the system is almost additive for the considered parameter-variation: all the defined objective functions [**] present $\sum_{i=1}^{N} S_{T_i}$ and $\sum_{i=1}^{N} S_i$ are respectively greater and less than 1 as they have to be (subsection IV.), but presenting a maximum value of 1.17 and minimum value of 0.88 respectively.

Finally, considering the 4^{th} combination, the main and total effect indices are evaluated for both the considered objective functions in order to select the parameters to be adopted for the UQ, i.e. those more influential; both the objective functions show that k_1, k_3 and d_1 are the most influential parameters including or not the longitudinal side slip in the model. This is illustrated in the bar plot of the total effect for all the parameters (Figure 20 and 21). Always for the sake of conciseness, just the mean of the adopted index related to the slope-objective functions is shown, that is

$$\overline{S}_{T_i} = \frac{1}{B} \sum_{b=1}^{B} (S_{T_i})_b \tag{17}$$

The obtained results are totally coherent with the *shimmy* phenomenon; the multi-body system presents a *shimmy* phenomenon primarily related to the lateral dynamics and the most influential parameters are exactly those that model the stiffness (k_1 and k_3) and damping (d_1) behavior of revoulte joints which have the rotation about the global y-axis as free. Regarding the *shimmy* phenomenon, it has been stated to be primarily lateral, since the lateral state δ and Δ always present the greatest amplitude at the LCOs generated by each of the analyzed point on all the determined branches. This means that the lateral mode is the one that most participates in the LCOs.

[**] Here, just the results for indices related to the 25^{th} slope are shown.

Parameter	Label	Maximum	Minimum	Units	PDF
Mass of the main fitting	M_{MF}	55.8	64.2	Kg	
Mass of the wheel axle	M_{WA}	93	107	Kg	
Mass of the wheel (left and right)	M_W	102.3	117.7	Kg	
Stiffness fuselage - main fitting	k_1	1395000	1605000	N m rad^{-1}	log-uniform
Stiffness main fitting - trail body	k_2	23250	26750	N m rad^{-1}	log-uniform
Stiffness trail body - wheel axle	k_3	697500	802500	N m rad^{-1}	log-uniform
Damping fuselage - main fitting of the left wheel	d_1	372	428	N m s rad^{-1}	log-uniform
Damping main fitting - trail body	d_2	372	428	N m s rad^{-1}	log-uniform
Damping trail body - wheel axle	d_3	372	428	N m s rad^{-1}	log-uniform
Inertia x (and y) axis - main fitting	$I1_{MF}$	0.1525	0.1755	kg m^2	uniform
Inertia z axis - main fitting	$I3_{MF}$	$5.7 \cdot 10^{-4}$	$6.5655 \cdot 10^{-4}$	kg m^2	uniform
Inertia x (and y) axis - wheel axle	$I1_{WA}$	0.0121	0.0139	kg m^2	uniform
Inertia z axis - wheel axle	$I3_{WA}$	$4.44 \cdot 10^{-5}$	$5.105 \cdot 10^{-5}$	kg m^2	uniform
Inertia x (and z) axis - wheel (right and left)	$I1_W$	6.51	7.49	kg m^2	uniform
Inertia y axis - wheel (right and left)	$I2_W$	10.23	11.77	kg m^2	uniform

Table 3: Parameters and the range of values adopted in the Sensitivity Analysis

Slip	$MAPE$ slope	$MAPE$ velocity
Pure	5.8	1.5
Combined	6.1	2

Table 4: Mean of $MAPE$ of the objective functions in terms of the slope and $MAPE$ of the objective function in terms of the velocity at the first identified point.

Keeping in mind the results obtained using the sensitivity indexes, the uncertainty quantification of the locus of Hopf bifurcation will be performed in terms of the three most influential parameters; the stiffness and the damping characterizing the revolute joint between the fuselage and the main fitting (k_1 and d_1) and the stiffness of the revolute joint between the trail body and the wheel axle (k_3).

C. Uncertainty Quantification

The parameters considered uncertain are those that have shown to be the most influential performing the sensitivity analysis, namely the stiffness and the damping characterizing the revolute joint between the fuselage and the main fitting (k_1 and d_1) and the stiffness of the revolute joint between the trail body and the wheel axle (k_3). The adopted variation for all of these is $\pm 10\%$ and this value has been selected to proof the accuracy of the developed method. Table 6 shows the adopted minimum and maximum values for all the three parameters.

The locus of Hopf bifurcation points are discretized using 31 points as done also performing the sensitivity analysis. The surrogate model adopted for the uncertainty quantification is the blind kriging. As stated in section **??** the percentage $T\%$ and the singular values (surrogate models) to be retained using the SVD and the HOSVD reduction

Combination	eq. f_0^2 and V		Combination	eq. f_0^2 and V	
1	13a	14a	7	13c	14b
2	13b	14a	8	13d	14b
3	13c	14a	9	13a	14c
4	13d	14a	10	13b	14c
5	13a	14b	11	13c	14c
6	13b	14b	12	13d	14c

Table 5: Combinations adopted to identify the best espression to be used for the total variance V.

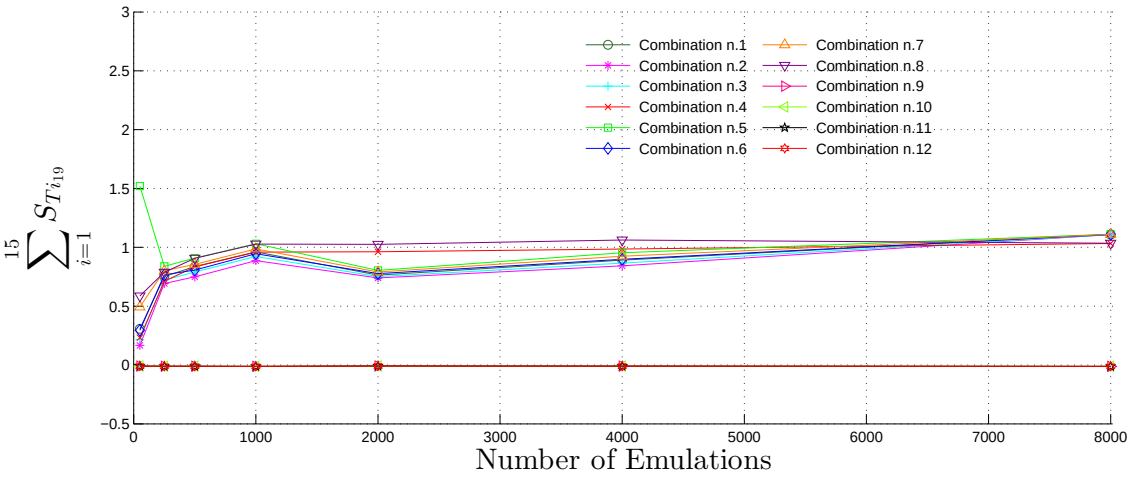

Figure 18: Comparison of 12 different evaluations of the total variance V considering the sum of the total effects S_{T_i} of the 25^{th} slope-objective function.

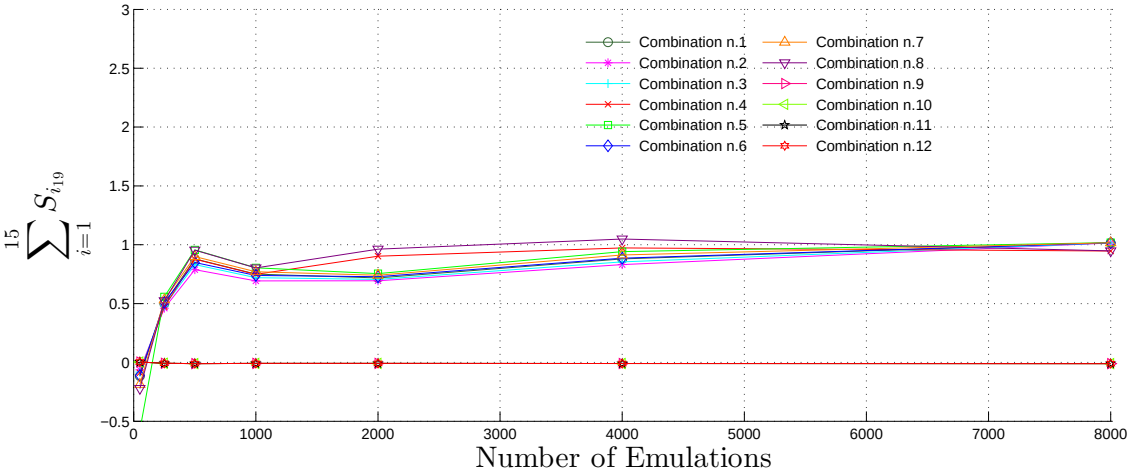

Figure 19: Comparison of 12 different evaluations of the total variance V considering the sum of the main effects S_i of the 25^{th} slope-objective function.

can be determined after having fixed the maximum acceptable error due to the rank reduction. The error metric here adopted is the Mean Average Percentage Error (MAPE), whose maximum value is fixed equal to 0.1%. Table 7 and 8 show the percentage $T\%$ and the singular values, i.e. the rank reduction and the number of surrogate models, to

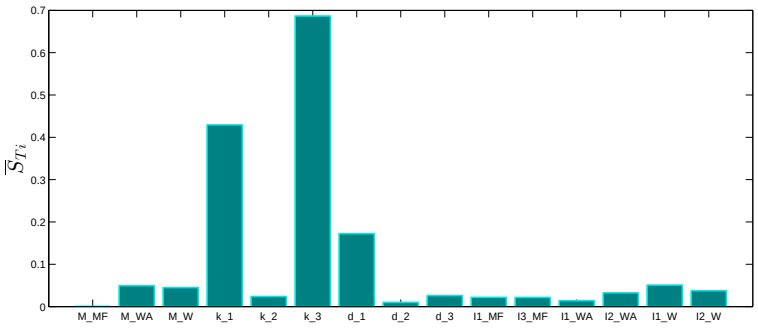

Figure 20: Comparison of the influence of each parameter on the output considering the mean of the total effect S_{T_i} related to the slope objective function and a pure side slip condition.

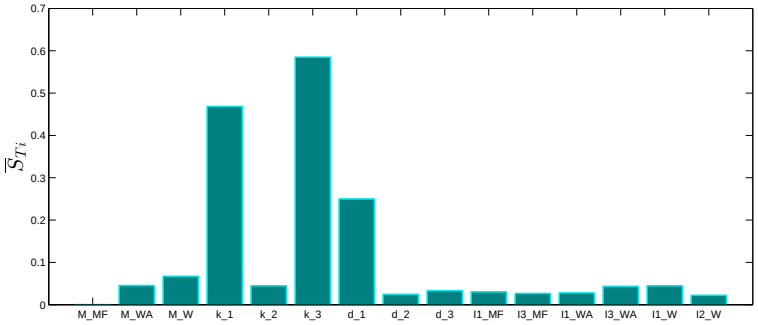

Figure 21: Comparison of the influence of each parameter on the output considering the mean of the total effect S_{T_i} related to the slope objective function and a combined side slip condition.

Parameter	Label	Maximum	Minimum	Units	PDF
Stiffness fuselage - main fitting	k_1	1350000	1650000	N m rad^{-1}	log-uniform
Stiffness trail body - wheel axle	k_3	675000	825000	N m rad^{-1}	log-uniform
Damping fuselage - main fitting of the left wheel	d_1	360	440	N m s rad^{-1}	log-uniform

Table 6: Parameters and the range of values adopted in the Uncertainty Analysis

be retained in order to fulfill the desired accuracy (MAPE ≤ 0.1) having considered the SVD or the HOSVD. The analysis shows that considering just a pure side slip, the same number of surrogate models must be trained whatever is the adopted decomposition, while including also the longitudinal slip more surrogate models are required if the HOSVD is adopted. Moreover, the presented results show that the proposed method to identify the rank reduction is more valid and 'stable' than the energy captured criterion. In fact, it is apparent that a priori such a high percentage of energy $T\%$ could not have been easily predicted as threshold at all. The world 'stable' is here used to characterize the proposed method in the meaning that changing the data set, the technique always work well in identifying the desired rank reduction even if the correspondent energy-threshold $T\%$ changes.

	SVD $\overline{W}_n$	SVD V	HOSVD
$T(\%)$	99.999999	99.99999	99.999999999
N model	5	8	13

Table 7: Comparison of rank reduction required using the SVD and the HOSVD having fixed the maximum acceptable error and considered a pure lateral slip.

The adopted iterative code to select the right number of singular values to be retained (and surrogate models to be

	SVD $\overline{W}_n$	SVD V	HOSVD
$T(\%)$	99	99.99999	99.9999999999
N model	2	6	10

Table 8: Comparison of rank reduction required using the SVD and the HOSVD having fixed the maximum acceptable error and considered a combined slip.

trained) gives very good results. 100 and 500 are the number of sampling points used to train and validate the adopted surrogate models respectively. Considering the 500 points validation sampling plane, Tables 9 and 10 show the mean of the MAPE in all the discretized points in terms of the forward velocity V and the vertical load $\overline{W}_n$ experienced by the nose landing gear, including or not the longitudinal slip.

	SVD $\overline{W}_n$	SVD V	HOSVD
0.35	0.40	0.41	0.86

Table 9: Validation of the surrogate models adopted for the UQ considering the tyre model the pure side slip. Mean of the MAPE for all the validation points and the 31 discretized points using the SVD and the HOSVD based method.

	SVD $\overline{W}_n$	SVD V	HOSVD
0.0086	0.2322	0.0086	0.1522

Table 10: Validation of the surrogate models adopted for the UQ including the longitudinal slip in the tyre model. Mean of the MAPE for all the validation points and the 31 discretized points using the SVD and the HOSVD based method.

Figures 22 and 23 present the results obtained performing the uncertainty quantification using the developed geometric based method and exploiting the HOSVD speed up process for both the analyzed slip conditions. In these Figures, the black dot points are the Hopf bifurcation points evaluated without using the time consuming numerical model, but the developed speed up process. Both the interval and probabilistic bounds are shown together with the area in which the LCO does or does not occur without any uncertainty. The uncertainty in the occurrence of LCO depends on the approach one wants to follow, i.e. interval or probabilistic one. Considering the interval approach, the results are more conservative and the uncertain region in which shimmy can occur wider. In fact, as previously stated, in the present analysis, the convex region described by the locus of Hopf bifurcations is where LCOs (shimmy phenomena) occur. The uncertainty related to this bound is wider if the lower and upper interval bounds are considered as shown in Figures 22 and 23. Adopting the probabilistic approach, one can select the lower and upper quantiles and then identify the uncertain 'tube' in which the locus Hopf bifurcations lies. The bounds of such an uncertain 'tube' are the lines corresponding to those obtained for the selected quantiles. For the sake of simplicity, nine values for the quantiles have been selected.

The performed uncertainty quantification, using the geometrical based method and the SVD/HOSVD technique, allows a reduction of 95% of computational time required by Monte Carlo Simulations .

Finally, Table 11 and 12 show a percentage comparison of the values assumed by the forward velocity V and the vertical load $\overline{W}_n$ at the different bounds of locus of Hopf bifurcation points. The error is computed between the results obtained adopting the SVD and the HOSVD as reduction technique. Mathematically, for a selected bound, the adopted formula is

$$\overline{S}_{T_i} = \frac{1}{B}\sum_{b=1}^{B}\frac{Par_{SVD_b} - Par_{HOSVD_b}}{Par_{HOSVD_b}} \tag{18}$$

where $Par_{\cdot_b}$ is the generic forward velocity V or vertical load $\overline{W}_n$ at the point with index b on the considered bound.

As it is apparent, the uncertain bounds obtained adopted either the SVD or the HOSVD based method are coherent one each other. It is important to remark that the uncertainty considered in the input parameters, even if just $\pm 10\%$, has a significant impact on the locus of Hopf bifurcation. Thus, it is significant considering a robust approach in order to reduce such and uncertainty and consider them in a design approach in order to eventually obtain a design that is robust in presence of uncertainty.

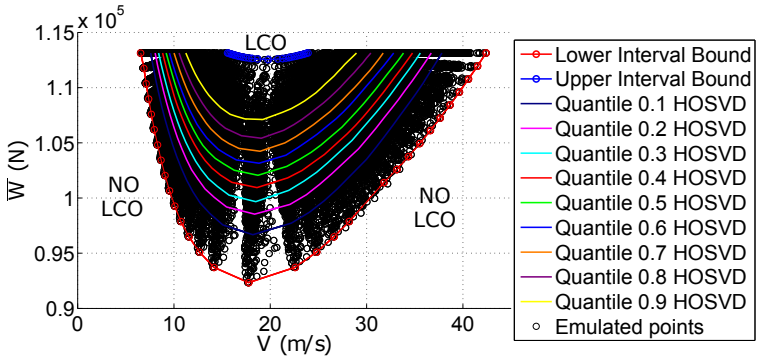

Figure 22: Uncertainty bounds evaluated using the geometric based approach, the HOSVD as the method for feature extraction and a pure side slip condition.

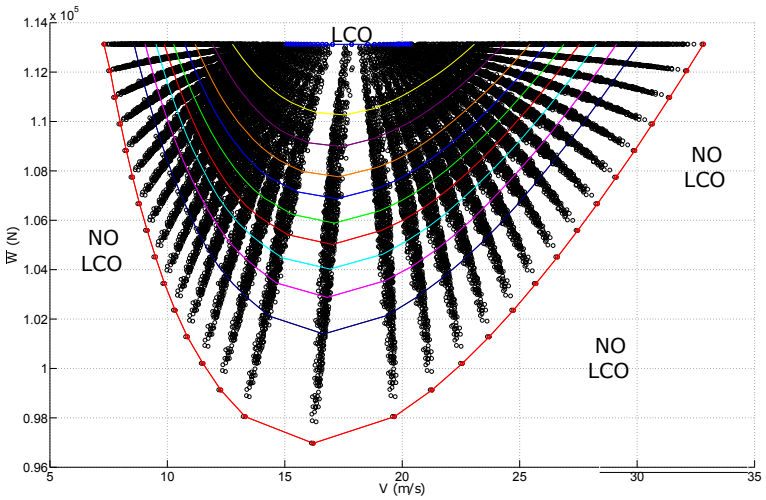

Figure 23: Uncertainty bounds evaluated using the geometric based approach, the HOSVD as the method for feature extraction and a combined slip condition..

MAPE (%)		
	$\overline{W}_n$	V
Lower Interval Bound	$2.89 \cdot 10{-}3$	2.98s
Upper Interval Bound	$3.62 \cdot 10{-}1$	1.37s
Quantile 0.1	$7.86 \cdot 10{-}1$	2.35
Quantile 0.2	$7.4 \cdot 10{-}1$	2.32
Quantile 0.3	$7.14 \cdot 10{-}1$	2.41
Quantile 0.4	$6.67 \cdot 10{-}1$	2.49
Quantile 0.5	$6.32 \cdot 10{-}1$	2.57
Quantile 0.6	$5.96 \cdot 10{-}1$	2.69
Quantile 0.7	$5.7 \cdot 10{-}1$	2.75
Quantile 0.8	$5.58 \cdot 10{-}1$	3.01
Quantile 0.9	$5.19 \cdot 10{-}1$	3.32

Table 11: Percentage comparison of the values assumed by the forward velocity V and the vertical load $\overline{W}_n$ on the determined uncertain bounds, using the SVD or HOSVD reduction and considering a pure lateral slip.

VII. Conclusions

An approach that enables a bifurcation analysis of multi-body structure has been described. The AUTO and LMS Virtual Lab Motion (VLM) software have been coupled, which enables stability analysis range and periodic orbit characterization of the nonlinear structure to be performed. An SVD based methodology was combined with the coupled software and used to predict the onset and characteristics of shimmy on a representative aircraft nose landing

MAPE (%)	$\overline{W}_n$	V
Lower Interval Bound	$3.88 \cdot 10{-}2$	0.33
Upper Interval Bound	$5.62 \cdot 10{-}2$	0.39
Quantile 0.1	$5.97 \cdot 10{-}2$	0.42
Quantile 0.2	$6.73 \cdot 10{-}2$	0.47
Quantile 0.3	$7.27 \cdot 10{-}2$	0.53
Quantile 0.4	$7.73 \cdot 10{-}2$	0.59
Quantile 0.5	$8.03 \cdot 10{-}2$	0.66
Quantile 0.6	$7.61 \cdot 10{-}2$	0.81
Quantile 0.7	$6.84 \cdot 10{-}2$	1
Quantile 0.8	$1.53 \cdot 10{-}2$	1.85
Quantile 0.9	$8.16 \cdot 10{-}2$	1.82s

Table 12: Percentage comparison of the values assumed by the forward velocity V and the vertical load $\overline{W}_n$ on the determined uncertain bounds, using the SVD or HOSVD reduction and considering a combined slip.

gear structure. Comparison with full time simulation results showed that the bifurcation approach was able to predict the stability bounds very accurately. Further applications of the approach enabled a sensitivity analysis to determine the most influential structural parameters and also to propagate and quantify the effects of uncertainty on the bifurcation characteristics. Significant computational savings were demonstrated with this approach.

Appendix

In this section the adopted expressions for the generalized forces acting on the wheels and the values of the coefficients used in the formulation are provided.

Normal load

$$F_{z_i} = p_{z1} \cdot \frac{F_{nominal}}{r_0} \cdot \rho_z \tag{19}$$

where ρ_z is the overall normal deflection and has been determined considering a tyre model with an elliptic contour of the cross section with a and b as semi-major and minor axes, respectively. $F_{nominal}$ is the nominal wheel load and has been fixed equal to half the vertical load $\overline{W}_n$. Labeling with W_{LG} the weight of the nose landing gear, the vertical load $\overline{W}_n$ is defined as

$$\overline{W}_n = W_{LG} - L \tag{20}$$

The other still undefined are given by

$$\begin{aligned}
&p_{z1} = 35 \qquad \rho_z = max((r_0 - r_1 - b + \xi) \cdot \cos(\gamma_i) + \eta \cdot \sin(\gamma_i), 0) \\
&\xi = b/(\sqrt{1 + (a/b)^2 \cdot \tan(\gamma_i)^2} \qquad \eta = a \cdot (a/b) \cdot \frac{tan(\gamma_i)}{\sqrt{1 + (a/b)^2 \cdot \tan(\gamma_i)^2}} \\
&a = R_c \qquad b = R_c/4 \qquad R_c = R_0/2
\end{aligned} \tag{21}$$

Longitudinal force in presence of pure longitudinal slip

$$\begin{aligned}
&F_{x_{0_i}} = D_{x_i} \cdot \sin(C_{x_i} \cdot \arctan(B_{x_i} \cdot k_i - \arctan(B_{x_i} - \alpha_{x_i}))) + S_{V_{x_i}} \\
&S_{V_{x_i}} = 0 \qquad B_{x_i} = \frac{K_{x_{k_i}}}{(C_{x_i} \cdot D_{x_i} + \epsilon_x)} \qquad C_{x_i} = p_{Cx1} \qquad D_{x_i} = \mu_{x_i} \cdot F_{z_i} \\
&E_{x_i} = (p_{Ex1} + p_{Ex2} \cdot df_{z_i} + p_{Ex3} \cdot df_{z_i}^2) \cdot (1 - p_{Ex4} \cdot sign(k_i)) \\
&\mu_{x_i} = (p_{Dx1} + p_{Dx2} \cdot df_{z_i}) \qquad K_{xk_i} = F_{z_i} \cdot (p_{Kx1} + p_{Kx2} \cdot df_{z_i}) \cdot \exp(p_{Kx3} \cdot df_{z_i})
\end{aligned} \tag{22}$$

Lateral force in presence of pure lateral slip

$$F_{y_{0_i}} = X_L \cdot D_{y_i} \cdot \sin(C_{y_i} \cdot \arctan(B_{y_i} \cdot \alpha_i - \arctan(B_{y_i} - \alpha_i))) + S_{V_{y_i}}$$
$$S_{V_{y_i}} = 0 \qquad B_{y_i} = \frac{K_{y_{\alpha_i}}}{(C_{y_i} \cdot D_{y_i} + \epsilon_y)} \qquad C_{y_i} = p_{Cy1} \qquad D_{y_i} = \mu_{y_i} \cdot F_{z_i}$$
$$E_{y_i} = (p_{Ey1} + p_{Ey2} \cdot df_{z_i}) \cdot (1 + p_{Ey5} \cdot {\gamma_i^*}^2 - (p_{Ey3} + p_{Ey4} \cdot \gamma_i^*) \cdot sign(\alpha_i) \qquad \mu_{y_i} = \frac{(p_{Dy1} + p_{Dy2} \cdot df_{z_i})}{(1 + p_{Dy3} \cdot {\gamma_i^*}^2)}$$
$$K_{yg0} = F_{z_i} \cdot (p_{Ky6} + p_{Ky7} \cdot dfz) \qquad K_{y\alpha_i} = p_{Ky1} \cdot F_{nominal} \cdot \frac{\sin(p_{Ky4} \arctan\left(\frac{F_{z_i}}{((p_{Ky2} + p_{Ky5} \cdot {\gamma_i^*}^2) \cdot F_{nominal})}\right)}{1 + p_{Ky3} \cdot {\gamma_i^*}^2} \quad (23)$$

Aligning Torque in presence of lateral slip

$$M_{z_0} = -t_{0_i} \cdot F_{y_{0_i}} + M_{zr0} \qquad M_{zr0} = 0$$
$$t_{0_i} = D_{t_i} \cdot \cos(C_{t_i} \arctan(B_{t_i} \cdot \alpha_i - E_{t_i} \cdot (B_{t_i} \cdot \alpha_{t_i} - \arctan(B_{t_i} \cdot \alpha_i)))) \cdot cos_a$$
$$B_{t_i} = (q_{Bz1} + q_{Bz2} \cdot df_{z_i} + q_{Bz3} \cdot df_{z_i}^2) \cdot (1 + q_{Bz5} \cdot |\gamma_i| + q_{Bz6} \cdot {\gamma_i}^2)$$
$$C_{t_i} = q_{Cz1} \qquad D_{t_i} = D_{t0_i} \cdot (1 + q_{Dz3} \cdot |\gamma_i| + q_{Dz4} \cdot {\gamma_i^*}^2 \qquad D_{t0_i} = F_{z_i} \cdot (\frac{r_0}{F_{nominal}} \cdot (q_{Dz1} + q_{Dz2} \cdot df_{z_i}) \cdot signV_{cx_i}$$
$$E_{t_i} = (q_{Ez1} + q_{Ez2} \cdot df_{z_i} + q_{Ez3} \cdot df_{z_i}^2) \cdot (1 + (q_{Ez4} + q_{Ez5} \cdot {\gamma_i}^*) \cdot \frac{2}{\pi} \cdot \arctan(B_{t_i} \cdot C_{t_i} \cdot \alpha_{t_i}))$$
$$K^*_{y\alpha_i} = K_{y\alpha_i} + \epsilon_k \qquad B_{r_i} = q_{Bz9} + q_{Bz10} \cdot B_{y_i} \cdot C_{y_i} \qquad C_{r_i} = 1$$
$$D_{r_i} = F_{z_i} \cdot r_0 \cdot (((q_{Dz6} + q_{Dz7} * df_{z_i}) + (q_D z8 + q_D z9 \cdot df_{z_i}) \cdot {\gamma_i}^* + (q_{Dz10} + q_{Dz11} \cdot df_{z_i}) \cdot {\gamma_i}^* \cdot |{\gamma_i}^*|) \cdot cos_a \cdot sign(V_{cx_i}) - 1) \quad (24)$$

Where $cos_a = \frac{V_{cx}}{V_{c_i} + epsilon_V}$

Forces acting on the landing gear in presence of combined slip

$$F_x = G_{x_{\alpha_i}} \cdot F_{x_0}$$
$$G_{x_{\alpha 0_i}} = \cos(C_{x_{\alpha_i}} \cdot \arctan(B_{x_{\alpha_i}} \cdot S_{Hx\alpha} - E_{x_{\alpha_i}} \cdot (B_{x_{\alpha_i}} \cdot S_{Hx\alpha} - \arctan(B_{x_{\alpha_i}} \cdot S_{Hx\alpha}))))$$
$$G_{x_{\alpha_i}} = \frac{\cos(C_{x_{\alpha_i}} \cdot \arctan(B_{x_{\alpha_i}} \cdot \alpha_i - E_{x_{\alpha_i}} \cdot (B_{x_{\alpha_i}} \cdot \alpha_i - \arctan(B_{x_{\alpha_i}} \cdot \alpha_i))))}{G_{x_{\alpha 0_i}}}$$
$$B_{x_{\alpha_i}} = (r_{Bx1} + r_{Bx3} \cdot {\gamma_i^*}^2 \cdot (\arctan(r_{Bx2} \cdot k_i))$$
$$C_{x_{\alpha_i}} = r_{Cx1} \qquad E_{x_{\alpha_i}} = r_{Ex1} + r_{Ex2} \cdot df_{z_i} \qquad S_{Hx\alpha} = r_{Hx1} \quad (25)$$

$$F_y = G_{y_{k_i}} \cdot F_{y_0} + S_{Vyk}$$
$$G_{y_{k0_i}} = \cos(C_{y_{k_i}} \cdot \arctan(B_{y_{k_i}} \cdot S_{Hxk} - E_{y_{k_i}} \cdot (B_{y_{k_i}} \cdot S_{Hxk} - \arctan(B_{y_{k_i}} \cdot S_{Hyk}))))$$
$$G_{y_{k_i}} = \frac{\cos(C_{y_{k_i}} \cdot \arctan(B_{y_{k_i}} \cdot k_i - E_{y_{k_i}} \cdot (B_{y_{k_i}} \cdot k_i - \arctan(B_{y_{k_i}} \cdot k_i))))}{G_{y_{k0_i}}}$$
$$B_{y_{k_i}} = (r_{By1} \cdot \cos(\arctan(r_{Bx2} \cdot (k_i - r_{By3})))$$
$$C_{y_{k_i}} = r_{Cy1} \qquad E_{y_{k_i}} = r_{Ey1} + r_{Ey2} \cdot df_{z_i} \qquad S_{Hyk} = r_{Hy1} + r_{Hy2} \cdot df_{z_i} \qquad S_{Vyk} = 0 \quad (26)$$

Aligning Torque in presence of combined slip

$$M_{z_i} = M^*_{z_i} + s \cdot F_{x_i}$$
$$M^*_{z_i} = -t_{eq_i} \cdot F_{y_i}$$
$$s = r_0 \cdot (s_{Sz1} + s_{Sz2} \cdot (\frac{F_{y_i}}{F_{nominal}})$$
$$t_{eq_i} = D_{t_i} \cdot cos(C_{t_i} \cdot \arctan(B_{t_i} \cdot \alpha_{eq_i} - \arctan(B_{t_i} \cdot \alpha_{eq_i})))) \cdot \cos(\alpha_i)$$
$$\alpha_{eq_i} = \sqrt{\alpha_i^2 + (\frac{K_{xk_i}}{K_{y\alpha_i}})^2 \cdot k_i^2)} \cdot sign(\alpha_i) \quad (27)$$

Overturning Couple

$$M_{x_i} = F_{z_i} \cdot r_0 \cdot (q_{Sx1} - q_{Sx2} \cdot {\gamma_i}^* + q_{Sx3} \cdot \frac{F_{y_i}}{F_{nominal}}) \tag{28}$$

Where F_{y_i} is fixed equal to $F_{y_{0_i}}$ if the pure lateral slip is considered.

Rolling Resistance Moment

$$M_{y_i} = -F_{z_i} \cdot r_0 \cdot (q_{Sy1} \arctan(\frac{V_{r_i}}{V_0} + q_{Sy2} \cdot \frac{F_{x_i}}{F_{nominal}}) \tag{29}$$

Where $V_{r_i} = V_{Cx_i} - V_{sx_i}$, $V_0 = \sqrt{g \cdot r_0}$ and F_{x_i} is fixed equal to $F_{x_{0_i}}$ if a pure longitudinal slip is considered.

Further definitions

$$\gamma_i^* = \sin(\gamma) \qquad df_{z_i} = (F_{z_i} - F_{nominal})/(F_{nominal}) \tag{30}$$

Adopted Coefficients

Tables 13 and 14 provides the adopted values for the coefficients.

Acknowledgments

The research leading to these results has received funding from the European Community's Marie Curie Initial Training Network (ITN) on Aircraft Loads Prediction using Enhanced Simulation (ALPES) FP7-PEOPLE-ITN-GA-2013-607911. The partners in the ALPES ITN are the University of Bristol, Siemens and Airbus Operations Ltd. The author wishes also to thank E. Coetzee for the helpful exchange of opinions.

References

[1]Conway, H. G., *Landing Gear Design*, Chapman & Hall, London 1958.

[2]Chai, S. T. and Mason, W. H., *Landing Gear Integration in Aircraft Conceptual Design*, September 1996 (rev. March 1997), $http://www.dept.aoe.vt.edu/\ mason/Mason_f/M96SC.html$ downloaded in April, 2015.

[3]Strogatz, S. H., editor, *Nonlinear Dynamics And Chaos: With Applications To Physics, Biology, Chemistry, and Engineering (Studies in Nonlinearity)*, Studies in Nonlinearity, Westview Press, 2nd ed., 2014.

[4]Currey, N. S., *Aircraft Landing Gear Design: Principles and Practices*, AIAA Education Series, Washington, 1988.

[5]Raymer, D. P., *Aircraft Design: A Conceptual Approach*, AIAA Education Series, Washington, June 1992.

[6]Doedel, E. and Oldeman, B., editors, *Auto-07p: Continuation and Bifurcation Software*, 2012, http://www.dam.brown.edu/people/sandsted/auto/auto07p.pdf downloaded in November, 2014.

[7]Howcroft, C., *A Bifurcation and Numerical Continuation Study of Aircraft Main Landing Gear Shiimmy*, PhD thesis, Department of Engineering Mathematics, University of Bristol, April 2013.

[8]Besselink, I. J. M., *Shimmy of Aircraft Main Landing Gears*, Department of Mechanical Engineering, Technische Universiteit Delft, 2000.

[9]Maas, J. W. L. H., *A comparison of dynamic tyre models for vehicle shimmy stability analysis*, Department of Mechanical Engineering, Technische Universiteit Windhoven, 2009.

[10]Sarkarv, S., Dong, A., and Gero, J. S., "Design Optimization Problem Reformulation using Singular Value Decomposition," *Journal of Mechanical Design*, Vol. 131(8), 2009.

[11]McGuinness, S., Armstrong, C. G., Murphy, A., Barron, J., and Hockenhull, M., "Improving Aircraft Stress-Loads Evaluation and Optimization Procedures," *2nd Aircraft Structural Design Conference,*, 2010.

[12]Ishteva, M., Absil, P. A., Huffel, S. V., and Lathauwer, L. D., "Best low multilinear rank approximation of higher-order tensors, based on the Riemannian trust-region scheme," *SIAM J.Matrix Anal. Appl.*, Vol. 32, No. 1, 2011, pp. 115-135.

[13]Tartaruga, I., Cooper, J. E., Sartor, P., Lowenberg, M. H., Coggon, S., and Lemmens, Y., "Efficient Prediction and Uncertainty Propagation of Correltated Loads," *SCITECH2015*, January 5-8 2015, Orlando, Florida USA.

[14]Tartaruga, I., Cooper, J. E., Lowenberg, M. H., Sartor, P., and Lemmens, Y., "Evaluation and Uncertainty Quantification of Bifurcation Diagram: Landing Gear, a case study," *UNCECOMP*, May 25-27 2015, Crete Island Greece.

[15]Tartaruga, I., Cooper, J. E., Lowenberg, M. H., Sartor, P., and Lemmens, Y., "Geometrical Based Method for the Uncertainty Quantification of Correlated Aircraft Loads," *submitted ASDJ*.

[16]http://www.plm.automation.siemens.com, date accessed June, 2015.

[17]Sobol', I. M., "Global sensitivity indices for nonlinear mathematical models and their Monte Carlo estimates," *Mathematics and Computers in Simulation*, Vol. 55, 2001, pp. pp 271–280.

[18]Saltelli, A., Chan, K., and Scott, E. M., editors, *Sensitivity Analysis*, Wiley, 1st ed., 2009.

[19]Omar, M. A., "Static Analysis of Large-Scale Multibody System Using Joint Coordinates and Spatial Algebra Operator," *Hindawi Publishing Corporation, The Scientific World Journal*, Vol. Article ID 409402, 2014, pp. 14 pages.

[20]Pacejka, H. B., *Tyre and Vehicle Dynamics*, Butterworth-Heinemann Ltd; 2nd Revised edition edition, 2006.

[21]Smiley, R. and Horne, W., "Mechanical properties of pneumatic tires with special reference to modern aircraft tires," 1958, Technical report, NACA TN 4110, Langley Aeronautical Laboratory, Langley Field.

[22]Tartaruga, I., Cooper, J. E., Lowenberg, M. H., Sartor, P., Coggon, S., and Lemmens, Y., "Prediction and Uncertainty Propagation of Correlated Time-Varying Quantities using Surrogate Models," *CAES Aeronautical Journal, DOI 10.1007/s13272-015-0172-1*.

Longitudinal Force		Lateral Force		Aligning Torque	
label	value	label	value	label	value
ϵ_x	0.1	ϵ_y	0.1	q_{Bz1}	8.964
p_{Cx1}	1.685	ϵ_k	0.1	q_{Bz2}	-1.106
p_{Dx1}	1.21	p_{Cy1}	1.193	q_{Bz3}	-0.842
p_{Dx2}	-0.037	p_{Dy1}	-0.99	q_{Bz5}	-0.227
p_{Ex1}	0.344	p_{Dy2}	0.145	q_{Bz6}	0
p_{Ex2}	0.095	p_{Dy3}	-11.23	q_{Bz9}	18.47
p_{Ex3}	-0.02	p_{Ey1}	-1.003	q_{Bz10}	0
p_{Ex4}	0	p_{Ey2}	-0.537	q_{Cz1}	1.180
p_{Kx1}	21.51	p_{Ey3}	-0.083	q_{Dz1}	0.1
p_{Kx2}	-0.163	p_{Ey4}	-4.787	q_{Dz2}	-0.001
p_{Kx3}	0.245	p_{Ey5}	0	q_{Dz3}	0.007
r_{Bx1}	12.35	p_{Hy1}	0.003	q_{Dz4}	13.05
r_{Bx2}	-10.77	p_{Hy2}	-0.001	q_{Dz6}	-0.008
r_{Bx3}	0	p_{Ky1}	-14.95	q_{Dz7}	0
r_{Cx1}	1.092	p_{Ky2}	2.13	q_{Dz8}	-0.296
r_{Ex1}	0	p_{Ky3}	-0.028	q_{Dz9}	-0.009
r_{Ex2}	0	p_{Ky4}	2	q_{Dz10}	0
r_{Hx1}	0.007	p_{Ky5}	0	q_{Dz11}	0
		p_{Ky6}	-0.92	q_{Ez1}	-1.609
		p_{Ky7}	-0.24	q_{Ez2}	-0.359
Lateral Force		r_{By1}	6.461	q_{Ez3}	0
X_L	0.05	r_{By2}	4.196	q_{Ez4}	.174
r_{Ey2}	0	r_{By3}	-0.015	q_{Ez5}	-0.896
r_{Hy1}	0.009	r_{Cy1}	1.081	s_{Sz1}	0
r_{Hy2}	0	r_{Ey1}	0	s_{Sz2}	0.001

Table 13: Adopted coefficiense for longitudinal and lateral force and aligning torque.

[23]Saitelli, T. H. . A., editor, *Global Sensitivity Analysis of Nonlinear Models, Importance Measures and Sobol' Sensitivity Indices*, Report

Overturning Couple		Rolling Resistance Moment	
label	value	label	value
q_{Sx1}	0	q_{Sy1}	0.01
q_{Sx2}	0	q_{Sy2}	0
q_{Sx3}	3.6		

Table 14: Adopted coefficiense for overturning couple and rolling resistance moment.

EUR 16052 EN, 1994, JOINT RESEARCH CENTRE EUROPEAN COMMISSION, Environment Institute.

[24]Saltelli, A., Annoni, P., Azzini, I., Campolongo, F., Ratto, M., and Tarantola, S., "Variance based sensitivity analysis of model output. Design and estimator for the total sensitivity index," *Computer Physics Communications*, Vol. 181, 2010, pp. pp 259–270.

[25]Saltelli, A., Ratto, M., Andres, T., Campolongo, F., Cariboni, J., Gatelli, D., Saisana, M., and S. Tarantola, title = Global Sensitivity Analysis, The Primer, p. . W. y. . ., editors.

[26]Nossent, J. and Bauwens, W., "Optimising the convergence of a Sobol sensitivity analysis for an environmental model: application of an appropriate estimate for the square of the expectation value and the total variance," *International Environmental Modelling and Software Society (iEMSs), International Congress on Environmental Modelling and Software Managing Resources of a Limited Planet, Sixth Biennial Meeting*, 2012, Leipzig, Germany.

[27]Iuliano, E. and Quagliarella, D., "Evolutionary Optimization of Benchmark Aerodynamic Cases using Physics-based Surrogate Models," *53rd AIAA Aerospace Science Meeting*, January 5-9 2015, Kissimmee, Florida USA.